11

# Time-Resolved Fourier Transform Infrared Emission Spectroscopy: Application to Pulsed Discharges and Laser Ablation

Svatopluk Civiš[1]*and Vladislav Chernov[2]
[1]*J. Heyrovský Institute of Physical Chemistry*
[2]*Voronezh State University*
[1]*Czech Republic*
[2]*Russia*

## 1. Introduction

### 1.1 Time-resolved Fourier transform infrared spectroscopy

Time-resolved spectroscopy (TRS) is a wide-spectrum technique used for studying the dynamics of chemical reactions, or the dynamic properties of molecules, radicals and ions in liquid, gas and solid states. In the infrared spectral range it can be achieved by using lasers (Smith & Palmer, 2002), grating spectrometers (Rödig & Siebert, 2002) or by interferometers (Masutani, 2002). The presented report is focused on the development and application of a time resolved system based on commercially available continuously scanning high resolution interferometer and its modification for time resolved Fourier transform spectroscopy (TR-FTS) (Kawaguchi et al., 2003).

The main advantage of TR-FTS lies in obtaining spectra in wide wavenumber intervals. The speed of data acquisition is limited by the duration of the acquisition process and by the band width of the used detector.

There are basically two ways of obtaining the time-resolved spectra: the continuous scan and the non-continuous, step scan (Masutani, 2002; Rödig & Siebert, 2002; Smith & Palmer, 2002). The continuous scan is best used when the duration of the observed phenomenon is longer than the time needed for carrying out one scan, *i. e.* for obtaining an interferogram up to the maximum trajectory difference (Rapid and ultrarapid scanning FT). Time-shifted individual scans provide a sequence of interferograms from which a conventional spectrum can be calculated. When using the rapid scanning and short distance mirror traversing, a time resolution from 1000 s to 1 ms can be reached.

A special approach to the time-resolved spectra of phenomena lasting from milliseconds to microseconds is the synchronous scanning FT technique (Kawaguchi et al., 2005). This method, as well as the methods mentioned below, requires the possibility of initiating the reaction in a pulse mode, *e. g.* using a laser, electric discharge, electron bombardment, a UV discharge lamp, *etc*. (Civiš et al., 2006). The apparatus carries out a continuous scan and, during the pulse, it reads the signal from the detector corresponding to the position

*Corresponding author. FAX: +420286591766; e-mail: civis@jh-inst.cas.cz

of the mirror and to the time from the beginning of the pulse reaction using the He–Ne laser fringe signals generated by the interferometer. This method is called stroboscopic interferometry (Smith & Palmer, 2002). After accumulating a sufficient amount of data and scans, the time-shifted interferograms are composed. The time mode is usually from 10 ms to 1 $\mu$s.

A more favorable method of non-continuous scanning in steps (step-scan) is achieved in discrete jumps and the time-resolved data from each position can be recorded after each transient event (Rödig & Siebert, 2002). Such a system is easy to couple with a pulse laser or a pulsed discharge. The step-scan spectrometers are commercially available and are used mainly for photolytic experiments in biology. The resolution of commercial step-scan type interferometers is limited to 0.1 $cm^{-1}$. A high resolution measurement with a step-scan type interferometer has been reported: a Connes type interferometer (CNRS Orsay) was used for the measurement of $N_2$ spectra with a resolution of 0.03 $cm^{-1}$ (Durry & Guelachvili, 1994).

### 1.2 Continuous scan systems: Synchronous triggering and data sampling

Continuously scanning spectrometers have been applied for time-resolved spectroscopy by several teams following the first report by Mantz (1976). Berg & Sloan (1993) developed a compact data acquisition system for submicrosecond time-resolved FTS. Nakanaga et al. (1993) applied a pulse discharge system to a continuously scanning interferometer without any modification of the system's software. The pulsed discharge was triggered by a He–Ne laser fringe signal with an appropriate delay time. The system was applied to the measurement of the time profiles of a vibration-rotation absorption spectrum of discharged CO. Recently, Kawaguchi et al. (2005) reviewed the methods of time-resolved Fourier transform infrared spectroscopy and its application to pulsed discharges and demonstrated the technique of FTS using a high-resolution Bruker IFS 120 HR supported by a microcontroller SX or Field Programmable Gate Array processor (FPGA) on $He_2$, ArH and $ArH^+$ spectra. The same system was used for studding the products of ArF excimer laser ablation products (Civiš et al., 2010; Civiš et al., 2010; Kawaguchi et al., 2008).

The continuous scanning principle was the basis for data acquisition by a modified (Bruker IFS 120) spectrometer in our laboratory at the J. Heyrovský Institute of Physical Chemistry, and a similarly modified spectrometer was used in Okayama (Japan).

The data acquisition system can be described as follows:

The position of the traversing mirror of the Michelson interferometer is detected by reading the interference maxima of the He–Ne laser emission. The input signal in a cosine function shape is digitally processed into rectangular pulses and becomes the internal standard of the interferometer. The frequency of these rectangular pulses depends on the mirror speed. In the classic measurement mode, the frequency is usually 10 kHz with a pulse duration of 100 $\mu$s. An external processor monitors the beginning of the He–Ne laser digital pulse, its order and the zero position of the mirror. During one pulse, the signal from the detector is read (30 or up to 64 readings), this is the so-called AD trigger Kawaguchi et al. (2008). These signals are shifted in time by $\Delta t$, where $\Delta t = 1$ or $2, 3 \ldots$ $\mu$s.

In this way, a matrix $I(t_k, \delta_i)$ of intensity $I$ in times $t_k$ is acquired for the given optical path difference $\delta_i$ ($i$ being the index of the selected optical path difference, from its zero to maximum values). A discharge pulse of variable length can be arbitrarily inserted into the data acquisition process (AD trigger). This process results in 30 to 64 reciprocally time-shifted interferograms.

Time resolved spectra are obtained by collecting data at various points between the zero-crossings and calculating the FT transformation for each such point. This system was utilized using a FPGA processor. The main role of the FPGA processor in our experiment was to create a discharge or laser pulse and AD trigger signals (the signal for data collection from the detector) synchronously with the He–Ne laser fringe signals from the spectrometer (see Figure 1 and Figure 2). The FPGA processor also controls the data transmission from the digital input board to the PC.

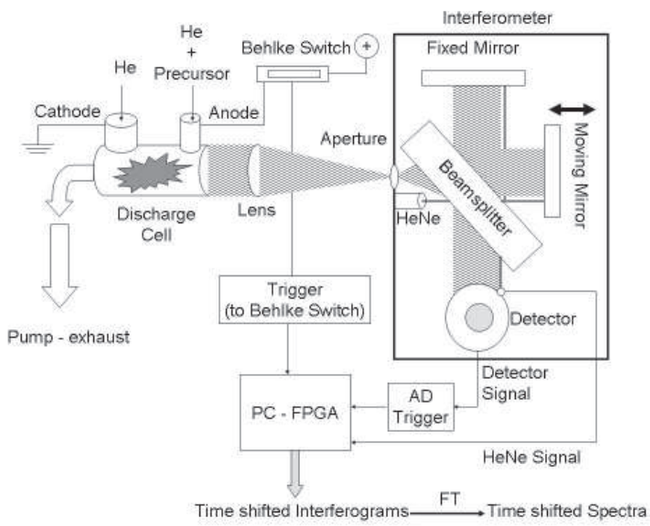


Fig. 1. A diagram of the time resolved Fourier transform spectrometer with FPGA microcontroller

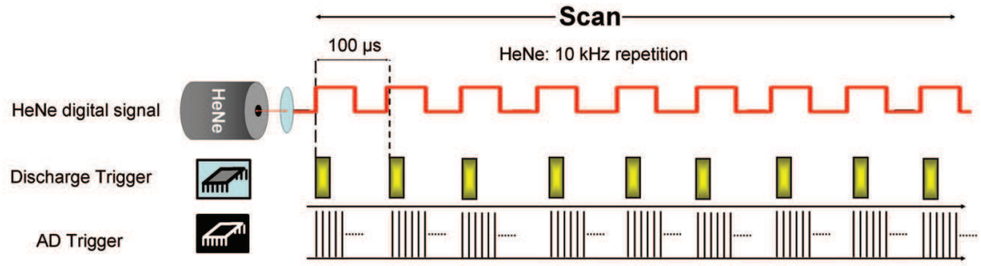


Fig. 2. Timing diagram for time resolved FT measurement. The scan and He–Ne fringe signals are supplied from Bruker 120 HR spectrometer. The velocity of the scanner is 10 kHz 100 $\mu$s time intervals are produced. The discharge trigger is programmed using FPGA microcontroller. Maximum 64 interferograms (64 time shifted spectra) can be obtained during one scan.

## 2. Continuous scan systems: application with discharges

Figure 1 depicts the experimental arrangement used in presented study. Infrared emission was observed from a pulsed discharge of FT time-resolved measurements. The parent compound hydrogen or $(CN)_2$ was entrained in an inert carrier gas (He, Ar) and entered in the 20 cm long positive column discharge (or hollow cathode) tube with an inner diameter of

12 mm. The pulsed discharge was induced by a high voltage transistor switch HTS 81 (Behlke electronic GmbH, Frankfurt, Germany) between the stainless steel anode and grounded cathode. The plasma produced from the reaction mixture was cooled by flowing water in the outer jacket of the cell. The best conditions for the generation of radicals or ions were found to be $p(\mathrm{He}, Ar) = 2$–10 Torr and 50 mTorr of parent molecules. The voltage drop across the discharge was 1000 V, with a pulse width of 20 or 40 $\mu$s and 0.5 A peak-to-peak current. The scanner velocity of the FT spectrometer was set to produce a 10 kHz He–Ne laser fringe frequency which was used to trigger the pulsed discharge. The recorded spectral range was 1800–4000 $cm^{-1}$ with an optical filter, and a unapodized resolution of 0.07 or 0.025 $cm^{-1}$. The 32–100 scans were coadded so as to obtain a reasonable signal-to-noise ratio. The observed wavenumbers were calibrated using CO ground state rotation-vibration lines presenting in the spectra (Guelachvili & Rao, 1986) as impurities.

### 2.1 He discharge plasma

#### 2.1.1 Introduction

The $He_2$ molecule is known as the first Rydberg molecule, since its spectrum was reported in 1913. Many spectroscopic studies have been carried out as compiled in a book of Huber & Herzberg (1979) and in the DiRef web site (Bernath & McLeod, 2001). Most of the spectra of $He_2$ molecule have been observed in the visible and ultraviolet regions. Ginter & Ginter (1988); Ginter et al. (1984) compiled and analyzed the energy levels of Rydberg states originating from the electronic configurations $(1\sigma_g)^2(1\sigma_u)np\lambda(^3\Pi_g, {}^3\Sigma_g^+)$ and $(1\sigma_g)^2(1\sigma_u)ns\sigma, nd\lambda(^3\Sigma_u^+, {}^3\Sigma_u^+, {}^3\Pi_u, {}^3\Pi_u)$ by multichannel quantum defect theory, where $n$ is the principal quantum number in the united atom molecular orbital designation. According to the energy levels listed in Refs. (Ginter & Ginter, 1988; Ginter et al., 1984), many electronic transitions are expected in the infrared region. However, observations of the infrared spectra so far have been limited to the three band systems below 8000 $cm^{-1}$:

(1) $b^3\Pi_g$–$a^3\Sigma_u^+$ with the 0–0 band origin at 4750$cm^{-1}$, studied by Hepner (1956), Gloersen & Dieke (1965), and (Rogers et al., 1988),

(2) $B^1\Pi_g$–$A^1\Sigma_u^+$ with the 0–0 band origin at 3501$cm^{-1}$, studied by Solka et al. (1987) and

(3) the $4f$–$3d$ band in 5100–5800 $cm^{-1}$ spectral region, studied by Herzberg & Jungen (1986).

The assignment of $4f$–$3d$ band was the first example concerning electronic states originating from the $f$-orbital electron.

The time-resolved Fourier transform spectroscopic system was applied for the observations of $He_2$ emission spectra produced by a pulsed discharge (Hosaki et al., 2004). This method has enabled us to observe many electronic transitions in the infrared region, including the previously reported bands. The spectroscopic analysis of newly observed three bands and their time profiles are briefly reported.

#### 2.1.2 Experimental

The spectra of $He_2$ were observed in emission from a hollow cathode discharge plasma. The hollow cathode stainless steel tube was 20 cm long with an inner diameter equal to 12 mm. The ac discharge was maintained by a high voltage transistor switch applied between the stainless steel anode and grounded cathode. The emission of $He_2$ has been also observed from a positive column, where lines from vibrationally excited states of $b^3\Pi_g$ were found to be more intense, compared with the case of the hollow cathode discharge. Here we report

only the spectra obtained from the hollow cathode discharge, because of its higher efficiency in the production of the highly excited electronic states of $He_2$.
The plasma made from a pure helium was cooled down by flowing water or by liquid nitrogen in outer jacket of the cell. The best conditions for the generation of the $He_2$ were found to be $p(He) = 1.33$ kPa (10 Torr).

### 2.1.3 Observed spectra and analysis

Figure 3 shows a part of the observed time-resolved emission spectrum from a discharge in He. The discharge was initiated at time zero and turned off at 20 $\mu$s. For AD-converter triggers, we used 3 $\mu$sec for the zero offset and interval values, that is, AD conversion occurs every 3 $\mu$sec from the start of the discharge and all together 30 pulses cover 90 $\mu$sec. The strong line (5880 cm$^{-1}$) in Figure 3 belongs to the He atomic line ($4d$–$3p$) and is observed as two intense peaks. It may be noted that the second peak appears after the discharge is off, that is, it is due to the afterglow plasma. The other spectral lines in Figure 3 pertain to the $4f$–$3d$ transitions of $He_2$ which have been analyzed by Herzberg & Jungen (1986).

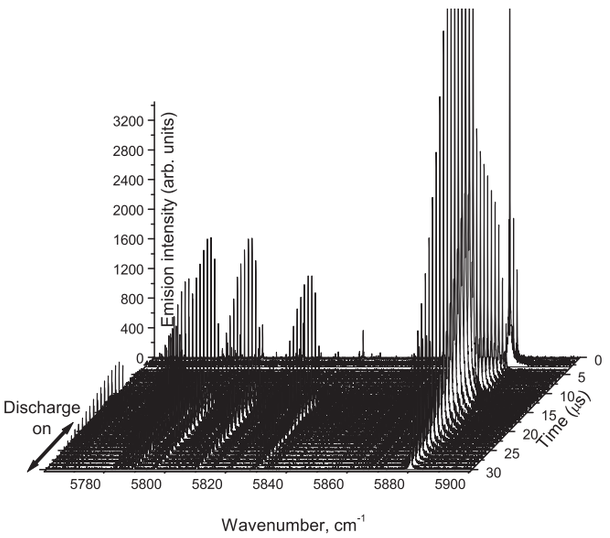


Fig. 3. A portion of the time-resolved spectrum observed by a pulse discharge in He with a pressure of 1.33 kPa (10 Torr). The discharge was applied in the interval of 0–20 $\mu$sec with a peak current of 0.5 A. The strongest peak belongs to atomic He line ($4d$–$3p$). Other lines pertain to $4d$–$3p$ transitions of $He_2$.

Figure 4 shows an observed spectrum in the 2750–5600 cm$^{-1}$ region, where we averaged all 30 spectra obtained by the time-resolved method. In the figure, the $b^3\Pi_g$–$a^3\Sigma_u^+$ $\nu = 0$–$0$ band is strongly observed in 4800 cm$^{-1}$ region. Most of spectral lines in the 5200–5900 cm$^{-1}$ region could be attributed to the $4f$–$3d$ band (Solka et al., 1987). In the 3300 cm$^{-1}$ region, the $B^1\Pi_g$–$A^1\Sigma_u^+$ $\nu = 0$–$0$ band found to be weak. From the time profile, it appears that the population in the singlet $B^1\Pi_g$ state decreased during the discharge period and increased in the afterglow, similarly to that observed for high-energy triplet states.

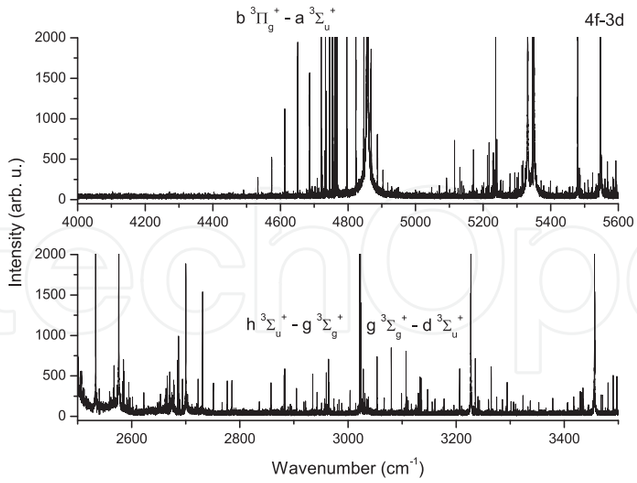


Fig. 4. An observed spectrum of $He_2$ in the 2750–5600 cm$^{-1}$, where 30 time-resolved spectra (90 $\mu$sec) are averaged. The discharge condition is given in the caption of Figure 3

In addition to these already reported bands, some new bands were observed. In the 3200 cm$^{-1}$ region, two series of lines have been observed with no $Q$-branch transitions. Rotational assignments are listed in Table 1 with the observed wavenumbers.

| $N$ | $P(N)$ | o.-c. | $R(N)$ | o.-c. |
|---|---|---|---|---|
| $h^3\Sigma_u^+$–$g^3\Sigma_g^+$ | | | | |
| 0 | 3177.5569 | 0.0006 | | |
| 2 | 3134.9969 | -0.0005 | 3206.4133 | 0.0018 |
| 4 | 3107.2556 | -0.0001 | 3235.5447 | 0.0000 |
| 6 | 3080.1473 | -0.0010 | 3264.8626 | -0.0064 |
| 8 | 3053.7916 | 0.0000 | 3294.3028 | 0.0089 |
| 10 | 3028.3000 | 0.0012 | 3323.7108 | -0.0054 |
| 12 | 3003.7698 | -0.0002 | 3353.0067 | 0.0013 |
| 14 | 2980.2783 | -0.0002 | | |
| $g^3\Sigma_g^+$–$d^3\Sigma_u^+$ | | | | |
| 1 | 3190.4064 | -0.0019 | 3232.9664 | -0.0013 |
| 3 | 3160.7770 | -0.0003 | 3259.9345 | 0.0005 |
| 5 | 3130.2548 | 0.0017 | 3285.6522 | 0.0016 |
| 7 | 3098.93068 | 0.0021 | 3130.0069 | 0.0006 |
| 9 | 3066.8917 | -0.0002 | 3332.8839 | -0.0017 |
| 11 | 3034.2243 | -0.0031 | 3354.1697 | 0.0005 |
| 13 | 3001.0169 | 0.0015 | | |

Table 1. Observed transitions of $He_2$ (cm$^{-1}$). $N$ denotes the rotational quantum number neglecting spin in lower electronic states.

The analysis using the standard energy level expressions gave the rotational and centrifugal distortion constants, and the band origin (term energy) as listed in Table 2.

| | Present | Previous |
|---|---|---|
| $(h^3\Sigma_u^+)$ | | $(a)$ |
| $B$ | 7.14853(24) | 7.149 |
| $D \times 10^3$ | 0.5053(24) | 0.574 |
| $H \times 10^7$ | −0.686(87) | |
| $E$ | | |
| $(g^3\Sigma_g^+)$ | | $(b)$ |
| $B$ | 7.096458(94) | 7.0968(1) |
| $D \times 10^3$ | 0.53071(44) | 0.538(7) |
| $E$ | 3204.8746(11) | |
| $(d^3\Sigma_u^+)$ | | $(c)$ |
| $B$ | 7.226364(88) | 7.2286(15)[a] |
| $D \times 10^3$ | 0.51991(37) | 0.532(3) |
| $E$ | 0.0 | 0.0 |

(a) Huber & Herzberg (1979)
(b) Orth & Ginter (1976)
(c) Ginter (1965)

Table 2. Molecular constants of $He_2$ in the $h^3\Sigma_u^+$, $g^3\Sigma_g^+$ and $d^3\Sigma_u^+$ states ($cm^{-1}$ units). Numbers in parentheses denote one standard deviation and applied to the last significant digits.

Spin splitting was not observed in these bands. The magnitude of the rotational constants was useful for identification of the electronic state. The band origin frequencies 3204.9 $cm^{-1}$ and 3194 $cm^{-1}$ of the two bands were consistent with those of the $g^3\Sigma_g^+$–$d^3\Sigma_u^+$ ($v = 0$–0) and $h^3\Sigma_u^+$–$g^3\Sigma_g^+$ ($v = 0$–0) transitions, respectively. Both the bands were identified for the first time in the infrared region, although electronic states involved have been observed by other electronic transitions in the visible region. Molecular constants determined in the previous studies are also listed in Table 2 for comparison.

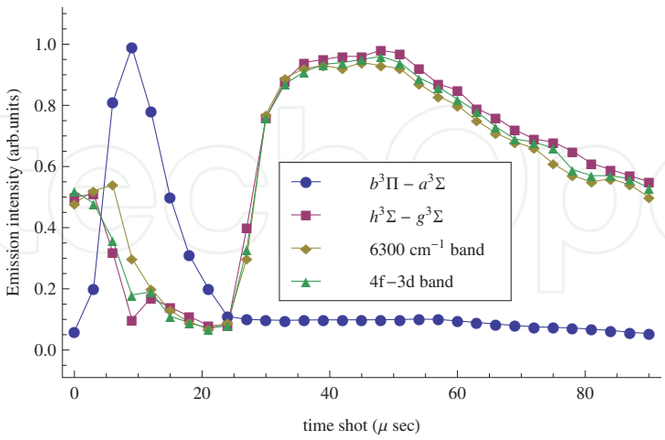


Fig. 5. Observed time profiles of emission intensities of $He_2$

Time profiles of observed spectral lines are depicted in Figure 5 for several bands. Except for the transitions from the $b^3\Pi$ state, the high-energy Rydberg states are produced strongly in

the afterglow plasma. This means those states are more fragile during the discharge period and may not be observed strongly in a normal DC discharge.
The pulsed discharge and multi-sampling system produce an interesting spectral feature of $He_2$ in the infrared region. Especially, when the data sampling is carried out after turning off the discharge, intense emissions from many electronic bands are strongly observed. The analysis may provide information about high-energy Rydberg states including states originating from $f$-orbital electrons.
Figure 6 shows the energy level diagram of $He_2$, where the energy values are represented relative to the $a^3\Sigma_u^+(v=0)$ state, which is located 144952 $cm^{-1}$ (18 eV) above the repulsive ground $X^1\Sigma_g^+$) state. The observed transitions are demonstrated by arrows.

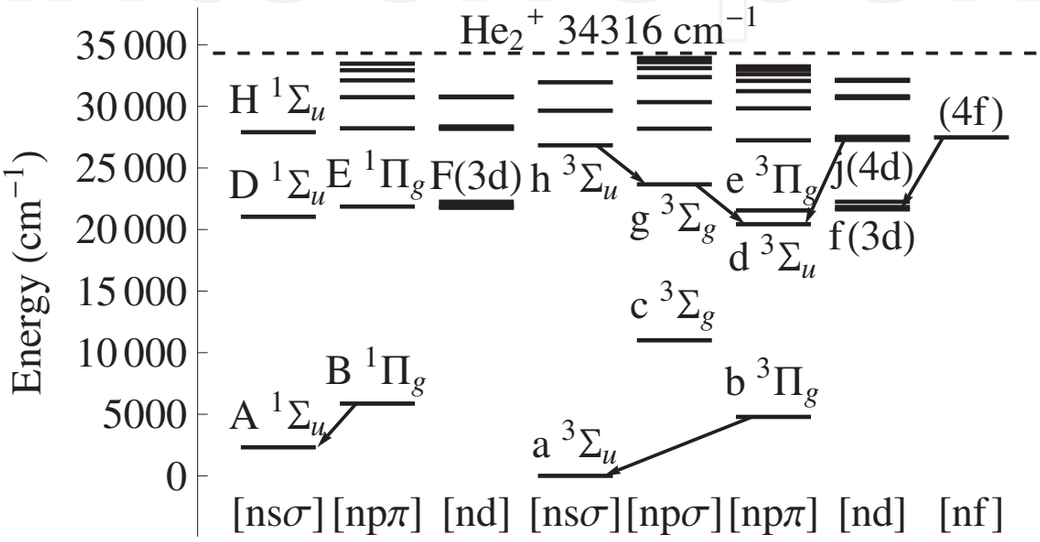


Fig. 6. Energy level diagram of $He_2$. The transitions observed in the present study are shown by arrows. The energy value is measured from the $a^3\Sigma_u^+(v=0)$ state; $n(>1)$ is the principal quantum number in a united atom molecular orbital designation. The ionization limit to $He_2^+$ is 34316 $cm^{-1}$.

### 2.2 Hydrogen containing discharge

Hydrogen and helium are the two most abundant elements in the universe. The hydrogen molecule and its various hydrides are the first source of aggregation and formation of interstellar matter. This process occurs in dense interstellar clouds, in star-forming regions and also in the atmosphere of some heavy planets (*e. g.*, Jupiter, Saturn,Uranus). The $H_3^+$ ion plays a dominant role in all these cases (Drossart et al., 1989; Herbst & Klemperer, 1973; McCall et al., 1998). After the first laboratory spectroscopic detection of $H_3^+$ (Oka, 1980), a large number of laboratory studies have been published, of which about 20 were concerned with measuring new infrared spectra, describing about 800 transitions from a variety of vibrational bands in the spectral range between 1800 and 9000 $cm^{-1}$. It is apparent from the comprehensive evaluation and compilation study of $H_3^+$ spectroscopy by Lindsay & McCall (2001) that most laboratory studies were carried out using absorption measurements. The only exception consists of the pioneering experiments of Majewski et al. (1987; 1994), who used a combination of a water-cooled, high-pressure, high-current emission hollow cathode together with an FT spectrometer. Majewski *et al.* used a high pressure of hydrogen gas (5–50 Torr)

and high discharge current (up to 2.5 A) for production of $H_3^+$. They obtained a very dense spectrum containing, in addition to $H_3^+$, a large number of H atomic, $H_2$ valence, $H_2$ Rydberg, $H_3$ neutral, and also other unidentified transitions.
In this part we describe the application to the observation of $H_3^+$, He and H emission produced by a pulsed discharge in a $He/H_2$ mixture in the infrared spectral range. The use of time-resolved FT spectroscopy opens new pathways and new points of view in the study of the formation and decay processes inside the discharge plasma and permits description of the dynamics of the formation and decay of excited states of the $H_3^+$ ion (Civiš et al., 2006).

### 2.2.1 Experimental

The emission spectra from a hollow cathode discharge plasma in $He/H_2$ mixtures were observed with the time-resolved Fourier transform high-resolution Bruker IFS 120 HR interferometer (Civiš et al., 2006). The hollow cathode stainless steel tube, covered with an outer glass jacket, was 25 cm long with an inner diameter of 12 mm. The $He/H_2$ plasma was cooled by liquid nitrogen in the outer jacket of the cell. The voltage drop across the discharge was 800 V, with a pulse width of 20 $\mu$s and 0.6 A peak-to-peak current The recorded spectral range was 1800–4000 $cm^{-1}$ with an optical filter, at an unapodized resolution of 0.1 $cm^{-1}$. Sixty-four scans were averaged to obtain a reasonable signal-to-noise ratio. The initial pressure of $H_2$ was 0.35 Torr and the He pressure was changed from 2 to 10.8 Torr.
The experiments were carried out with pulsed discharge with a width of 20 $\mu$s. Because of the high pressures (up to 10 Torr) required for generation of $H_3^+$ and thus, subsequently, the short relaxation times of the $H_3^+$ ions, the measurement was carried out with maximum time resolution of 1 $\mu$s, which is currently limited by the response time of a preamplifier of the InSb detector. Compared to previous measurements (Hosaki et al., 2004; Kawaguchi et al., 2003), the data acquisition system was modified for enabling recording of 64 time-shifted spectra in a single scan.

### 2.2.2 Results and discussion

Helium has a higher ionization potential than $H_2$ (24.6 eV and 15.4 eV correspondingly; see Huntress, 1977), so that the electron temperatures are higher when He predominates in the discharge. Because of the low proton affinity of He (1.9 eV) compared to $H_2$ (4.5 eV), the He buffer is chemically quite inert.
The low temperature emission spectra from a hollow cathode discharge in a $He/H_2$ mixture were found to contain only several of the low $J$ and $K$ transitions of $H_3^+$, together with the atomic lines of He and H. No further lines of $He^+$, $H^+$ or molecular lines of $H_2$ or of neutral $H_3$ which also absorb in this area, were found (Davies et al., 1990; Vervloet & Watson, 2003). Figure 7 shows part of the observed time-resolved emission spectra of He (2129.83 $cm^{-1}$) and H (2148.79 $cm^{-1}$). Figure 7(b) depicts the $H_3^+$ line $Q(1,0)$ at 2529.724 $cm^{-1}$, which belongs to $\nu_2 = 1 \rightarrow 0$ band.
Figure 8 shows time profiles of emission lines of He (a,b), $H_3^+$ (c) and H (d). The absolute energy levels and Einstein coefficients $A_{ij}$ for He, H and $H_3$ were taken from the NIST database (Ralchenko et al., 2008) and from (Kao et al., 1991). The vertical axis shows observed intensity divided by the Einstein coefficients $A_{ij}$ and corresponds to the abundance in the upper state of the transition. It is noted that the emission from $n = 5$ of H was observed through the $n = 5$–4 transition, but other transitions from $n = 5$ are not observed because of the limited frequency range. Therefore, the abundance in the initial state of atomic transitions should be multiplied by a factor of 6 in the case of hydrogen. This sequence of processes was

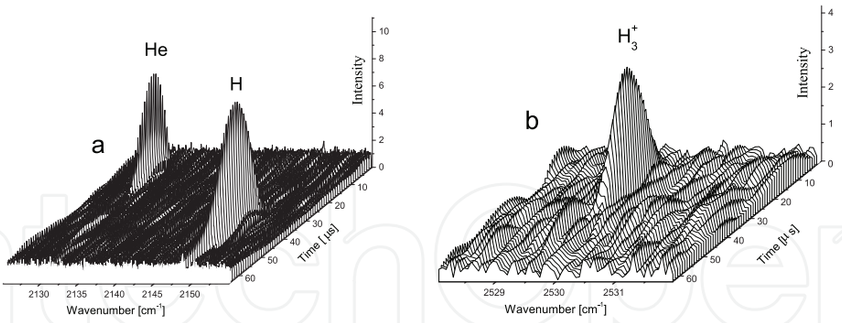


Fig. 7. Time-resolved infrared spectrum at 2125–2155 $cm^{-1}$ (a) and 2528–2532 $cm^{-1}$ (b), observed in a pulsed discharge in a He (10.8 Torr)/$H_2$ (0.4 Torr) mixture. The discharge was applied in a time interval of 0–20 $\mu$s with a peak current of 0.5 A.

observed for all the lines in the spectrum; the time in which the maximum emissions were measured for the individual transitions of the same species (He, $H_3^+$ and H) did not differ by more than $\pm 2$ $\mu$s.

Chemical processes in He/$H_2$ plasma that can lead to the formation of $H_3^+$ are discussed extensively in literature (Eqns. 1–4; see Plašil et al. (2002)):

$$\mathrm{He} + \mathrm{e_{fast}} \longrightarrow \mathrm{He}^* + \mathrm{e_{slow}} \qquad \sigma = 4 \times 10^{-18}\ \mathrm{cm}^2 \quad \text{for He}(2^3S) \tag{1}$$

$$\mathrm{He}^* + \mathrm{H_2} \longrightarrow \mathrm{H_2}^+ + \mathrm{e} \qquad \sigma = 2.6 \times 10^{-16}\ \mathrm{cm}^2 \quad \text{for He}(2^3S) \tag{2}$$

$$\mathrm{H_2} + \mathrm{e_{fast}} \longrightarrow \mathrm{H_2}^+ + \mathrm{e_{slow}} + \mathrm{e_{slow}} \qquad \sigma = 10^{-16}\ \mathrm{cm}^2 \quad \text{for electron energy of 70 eV} \tag{3}$$

$$\mathrm{H_2}^+ + \mathrm{H_2} \longrightarrow \mathrm{H_3}^+ + \mathrm{H} \qquad k = 2.0 \times 10^{-9}\ \mathrm{cm}^3\,\mathrm{s}^{-1}, \quad \Delta H = -1.65\ \mathrm{eV} \tag{4}$$

In all our experiments no emission from $H_3^+$ has been detected in pure hydrogen discharge. Reaction (4) is exothermic to have enough energy to produce $H_3^+$ in $\nu_2 = 1$ state. However, since $H_2$ is known to be efficient for relaxing the vibrational excited state, the vibrationally excited $H_3^+$ in pure $H_2$ discharge will be relaxed by the collision with $H_2$. It should be noted that the obtained radiative lifetime of $H_3^+$ is about 10 ms.

By adding a large amount of He the vibrational relaxation will be suppressed, and the $H_3^+$ emission becomes strong. At low helium pressures, $H_3^+$ is formed directly in the discharge through direct ionization of $H_2$ and subsequent processes (Eqns. 1,4). Formation and decay of excited $H_3^+$ occurs in $\mu$s time range. The calculated values for the deactivation rate $k_{ij} = (2..5) \times 10^5\ \mathrm{s}^{-1}$ are several orders of magnitude higher than the Einstein coefficients $A_{ij}$ for spontaneous emission of $H_3^+$, and recombination process described later, which clearly demonstrates the efficiency of collision processes for deactivation of the $H_3^+$ excited states. In Figure 8, the second weaker maximum of the $H_3^+$ line was found at $45 \pm 2$ $\mu$s. This appears as a consequence of collisions of $H_2$ and metastable He with a long lived lifetime, as shown in Eqns. (2) and (4).

The entire process in the afterglow is concluded by formation of H, which could be observed on two lines (2148.7 and 2467.8 $cm^{-1}$) at times of 40–60 $\mu$s (Figure 8d). The two lines corresponding to transitions in excited atomic hydrogen were observed with two peaks (Figure 8d): a small peak at 12 $\mu$s and a high-intensity peak with a maximum at $39 \pm 1$ $\mu$s. The former peak may be explained by direct dissociation of $H_2$ through collision with electron. We

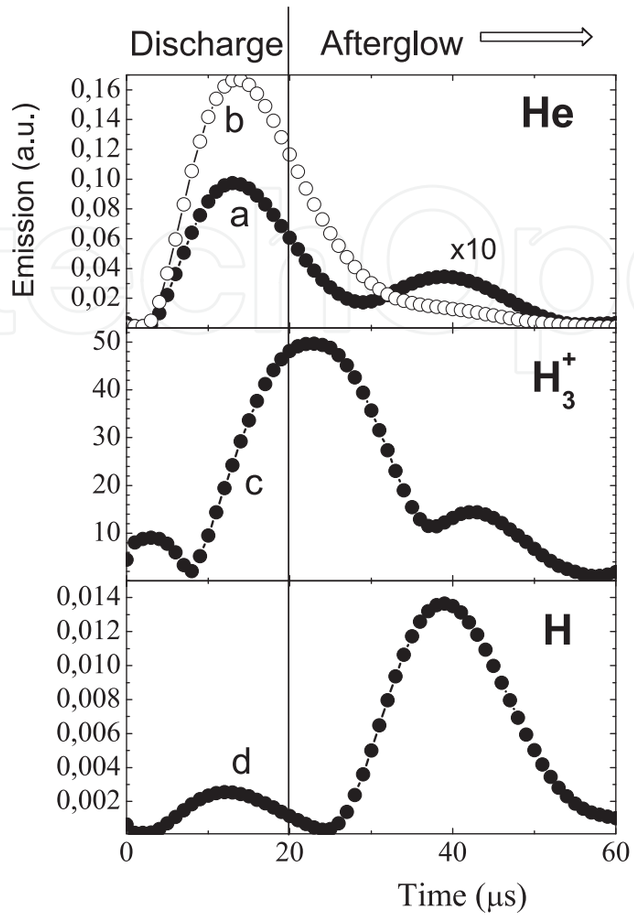


Fig. 8. Time-resolved emission profiles: (a) excited He $5f^1F^o$–$4d^1D$ transition at 2474.64 cm$^{-1}$ (magnified by ten), (b) He $3p^3P^o$–$3s^3S$ transition at 2327.77 cm$^{-1}$ (strongest line in the FTIR spectrum), (c) $H_3^+$ transition $Q(1,0)$ at 2529.72 cm$^{-1}$ and (d) H Brackett $\alpha$ ($n = 5$–4) at 2467.60 cm$^{-1}$. The absolute intensity of emission was corrected by the corresponding Einstein coefficients $A_{ij}$.

expect that the second peak is due to hydrogen atom produced by recombination of $H_3^+$ with electron.

When the discharge is turned off, the electron energy becomes lower through collision, and the recombination rate will be increased. The recombination products of the reaction of $H_3^+$ with an electron are either three neutral hydrogen atoms or a hydrogen molecule together with a hydrogen atom. For the most important case of near-zero initial energy, *i. e.*, low-energy electrons and small internal excitation of the $H_3^+$ ion, the two reaction channels can be expected (Eqns. 5,6) (Motret et al., 1985; Strasser et al., 2002).

$$H_3^+ + e^- \longrightarrow H_2(X^1\Sigma_g^+, vJ) + H(1s), \quad \Delta E = 9.2\ \text{eV} \tag{5}$$

$$\longrightarrow H(1s) + H(1s) + H(1s), \quad \Delta E = 4.8\ \text{eV} \tag{6}$$

We observed two atomic H transitions in our spectra after electron recombination of $H_3^+$ (Figure 8); both originated from energy levels above 13 eV. This is more than the kinetic energy released in an energetically more advantageous process (Eq. 6). Because of the high pressure of He, excitation of H atoms can be expected in collisions with excited He atoms in the early afterglow.

### 2.3 $(CN)_2$-containing discharge

The CN free radical is observed in interstellar molecular clouds and the atmospheres of stars, planets and comets. It is also significant in numerous laboratory processes at high temperatures (flames, chemical reactions, discharges) where it is often formed from trace amounts of carbon and nitrogen. It is a very strong absorber/emitter of radiation and its spectra, extending from the vacuum UV far into the infrared without significant gaps, provide a very useful tool for its detection and monitoring. A vast proportion of the available spectral data arises from the $A^2\Pi$–$X^2\Sigma^+$ and $B^2\Sigma^+$–$X^2\Sigma^+$ electronic transitions (Prasad & Bernath, 1992; Ram et al., 2006) and the infrared transitions in the $X^2\Sigma^+$ ground electronic state (Cerny et al., 1978; Horká et al., 2004). In our previous paper (Horká et al., 2004) we concentrated primarily on the measuring and analysis of $^{12}C^{14}N$ vibration-rotation bands for the sequences $\nu = (1\text{–}0)$ through (9–8) which were observed in the spectral region 1800–2200 cm$^{-1}$ with Fourier Transform spectroscopy. From the point of view of the vibrational excitation, the most important information is obtained from vibronic data involving vibrational levels up to $\nu = 18$ (Ram et al., 2006). Such high vibrational excitation corresponds to temperatures well above 45000 K thus indicating the potential use of CN in high temperature monitoring and the possibility of experimental determination of the molecular potential energy function (Horká et al., 2004).

Cerny et al. (1978) analyzed fourteen vibronic bands of the $\Delta\nu = 1, 0, -1, -2$ spread out in the near infrared spectral range with $\nu' = 0$ to 4 for $A^2\Pi$ electronic state. Kotlar et al. (1980) carried out a perturbation analysis of data taken at the University of Berkeley, to give a deperturbed set of the constants for the $\nu = 0$ to $\nu = 12$ vibrational levels of the $A^2\Pi$ state. Prasad & Bernath (1992) measured and analyzed the red system of CN by using a jet-cooled corona excited supersonic expansion in a spectral range of 16500–22760 cm$^{-1}$. They measured a total of 27 bands with $\nu' = 8$ to 21 for $A^2\Pi$ electronic state. Furio et al. (1989) used the laser fluorescence excitation spectra for the measurement of the $B^2\Sigma^+$–$A^2\Pi(\nu = 8, 7)$ band in the 20400 cm$^{-1}$ spectral range and derived the constants for $\nu = 7$ of the $A^2\Pi$ state. Rehfuss et al. (1992) used an FT spectrometer in the ultraviolet, visible and infrared region for a measurement of the CN spectrum. A total of 54 bands were observed throughout the red and infrared region from 16000 to 2500 cm$^{-1}$. The observed sequences include $\Delta\nu = +4$, $+3$, $+2$, $+1$, 0, $-1$, $-2$ and $-3$ with vibrational levels up to $\nu = 14$, where some sequences were not observed, due to small Franck–Condon factors and/or sensitivity of the spectrometer.

The 0–0 band of the $A^2\Pi$–$X^2\Sigma^+$ system appears at 9117 cm$^{-1}$. Since the vibrational frequency of CN is about 2042 cm$^{-1}$ and 1813 cm$^{-1}$ in the $X^2\Sigma^+$ and $A^2\Pi$ respectively, the $\Delta\nu = -1$, $-2$ and $-3$ sequences occur near 7000, 5000 and 3000 cm$^{-1}$ respectively. In the region between 5000 and 2000 cm$^{-1}$, the vibronic transitions are rather unfavorable due to the Franck-Condon factors of 0.15–0.05 Prasad & Bernath (1992); Sharp (1984). Furthermore one loses, compared with the 0–0 band, at least an additional factor of 20 due to the $\nu^3$ dependence in the Einstein $A$ coefficient. Thus a high resolution vibronic CN spectrum with a good signal-to-noise ratio for the $\nu = 3$ sequence band region has not been reported until now. Only a low resolution spectrum was weakly observed by Rehfuss et al. (1992).

There is still a gap for the high resolution measurement and detailed analysis of the spectral bands concerning $\nu = 5$ to 6 of the $A^2\Pi$ state. The turning point in this measurement of CN in the infrared spectral range was the introduction of time resolved FT spectroscopy (Civiš et al., 2008). This method makes it possible to distinguish the weak emission (or absorption) bands from strong bands appearing in the spectrum if the time profiles are different. In the case of CN, weak vibronic bands in the 5 $\mu$m region were separated from strong long lived vibration-rotation bands. In this part a spectroscopic analysis of 7 newly observed $\Delta\nu = -3$ sequences bands: 0–3, 1–4, 2–5, 3–6, 4–7, 5–8 and 6–9 of the $A^2\Pi$–$X^2\Sigma^+$ transition is reported.

### 2.3.1 Observed CN spectra and their analysis

Figure 9 shows a part of the time-resolved FT spectra of emission from a discharge in a $(CN)_2$ and He mixture, where the discharge pulse width was 20 $\mu$s. Thirty time-resolved spectra were obtained in one measurement with a time-interval of 3 $\mu$s, and 6 spectra are shown in Figure 9.

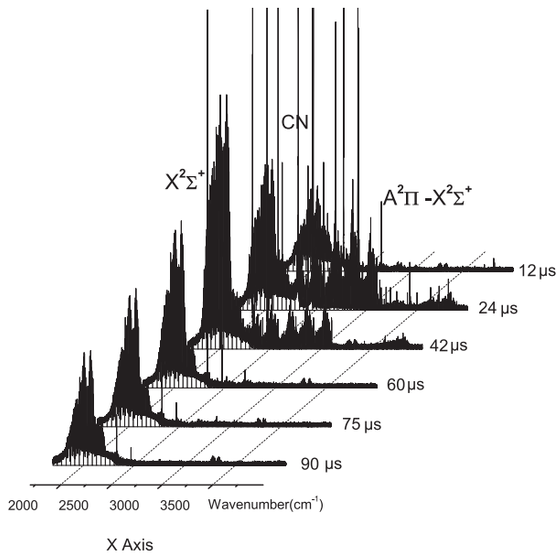


Fig. 9. The time-resolved emission FT spectrum from a pulsed discharge in a $(CN)_2$ and He mixture. The discharge pulse duration was 20 $\mu$s. The 30 time-resolved spectra were collected from $t = 0$–90 $\mu$s with a step of 3 $\mu$s. The spectra of $C_2H_2$ and $C_2$ were observed at 3300 and 3600 cm$^{-1}$.

The variation in intensity of the vibrational bands in the $X^2\Sigma^+$ state is low. On the other hand, relaxation of electronic transitions is as fast as expected from a short radiative lifetime. The wavenumber resolution of Figure 9 was 0.07 cm$^{-1}$, which was found to be insufficient for the analysis of the majority of the electronic transitions, because in the band-head region, the lines remained unresolved and the fit of the spectra was unsatisfactory.
In another time-resolved measurement we used a 0.025 cm$^{-1}$ resolution with a long discharge pulse (40 $\mu$s) in order to reach the maximum excitation and to set the system into a "steady state". The data collection system was set using the offset time of 5 $\mu$s before the end of the pulse and the spectra were taken in 1 $\mu$s intervals. A series of experiments was carried out under this condition, while the basic parameters of the discharge, He pressure

and discharge current were varied. A series of time-resolved FT spectra was measured in time intervals of 1–30 $\mu$s, providing the time profile of CN relaxation from the $A^2\Pi$ state to the ground electronic state. The time-scale was short for the study of the relaxation of the vibration-rotation transitions in the ground electronic state, but is enough for observations of relaxation of atomic He, N, C lines, and the $C_2$ radical. From this vast complex spectra, the spectrum No. 15, as shown in Figure 10, was chosen for the present spectroscopic analysis, which was obtained 10 $\mu$s after the end of the discharge. Figure 11 shows typical time-profiles of a vibration-rotation transition in the $X^2\Sigma^+$ state and a vibronic transition of CN, together with the atomic lines. The lifetime of the $A^2\Pi$–$X^2\Sigma^+$ transition is an order of 10 $\mu$s. However, the vibrational relaxation of CN in its ground state is significantly longer; even at a time of 25 $\mu$s after the discharge, the intensity of the vibrational fundamental band is still rising. The intensity of the He atomic line (2469.7 cm$^{-1}$) shows a fast decay, and lines of C and N atoms also relax with a speed comparable with atomic helium.

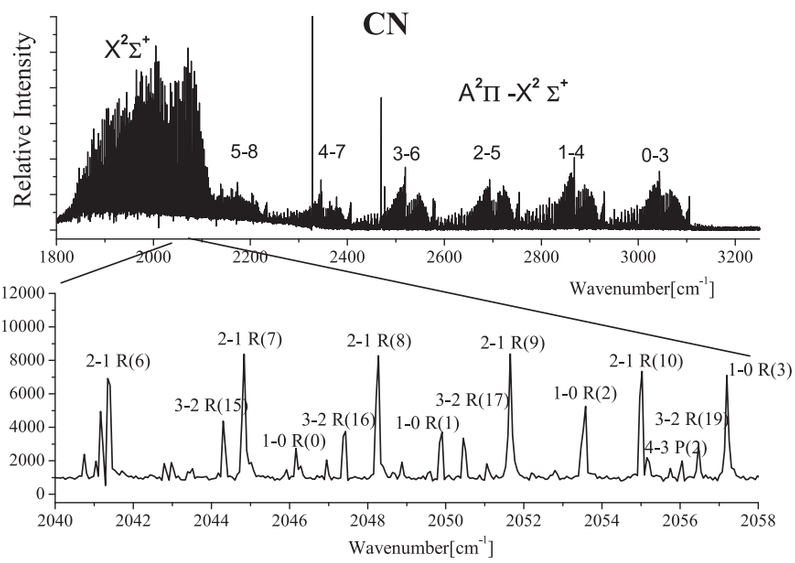


Fig. 10. The emission spectrum of the CN radical in the spectral range 3–5 $\mu$m. The overall view of the CN $A^2\Pi$–$X^2\Sigma^+(\Delta\nu = -3)$ sequence with the 1–0 fundamental electronic vibration–rotation band present with a band origin at 2042 cm$^{-1}$ and the other hot bands.

The rotational assignments of the $A^2\Pi$–$X^2\Sigma^+$: 0–3, 1–4, 2–5, 3–6, 4–7 bands were carried out according to the transition frequency calculations using molecular constants reported by Cerny et al. (1978). The $v = 5$–8 and 6–9 bands were assigned by molecular constants from Kotlar et al. (1980) who reported the Dunham parameters. The standard deviation of the fitting was 0.0009 cm$^{-1}$.

The time-resolved experiment itself was carried out in a wide range of time scales and with various discharge pulse lengths, thus enabling a complex study of the relaxation processes of the CN system in helium. Such a pulsed discharge gives a stronger emission for the $\Delta\nu = -3$ bands, compared with that of a DC discharge. In this study emission from the $\nu = 5$ and 6 vibrational levels of the $A^2\Pi$ state was observed for the first time. The observed intensity of each band was plotted against the energy value of the upper state of the transition to give a vibrational temperature of 6700 K for the $A^2\Pi$. The value does not change significantly after 10 $\mu$sec, because the vibrational relaxation is not fast. Similarly the vibrational temperature is

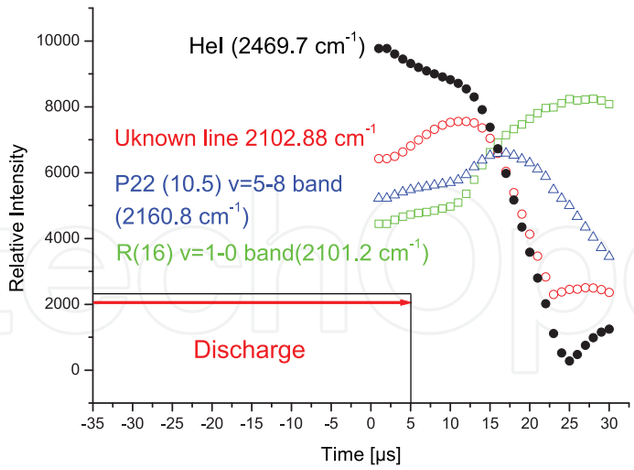


Fig. 11. Time-profiles of the He(I) atomic line, P22 (10.5) line of the $A$–$X$, 5–8 band and R(16) line of the 1–0 fundamental vibration-rotation band, and nitrogen atomic line. The discharge pulse was 40 $\mu$s long. The time-resolved spectra were collected after 35 $\mu$s (5 $\mu$s before the end of the discharge pulse) with a step of 1 $\mu$s.

found to be 6757±534 K for the $X^2\Sigma^+$. Using the vibrational temperatures, we estimated the abundance of the $A^2\Pi$ to be 0.58% of that of the $X^2\Sigma^+$.

### 2.4 Other examples

A discharge in a hydrogen-containing mixture can produce hydrides whose spectra can be registered using Fourier transform spectroscopy. One of then goals of such studies is simulation of potential high energy processes in early Earth's atmosphere (as meteorite impact, lightning), which could lead to more complex compounds generated from simple molecular gases. (Babánková et al., 2006). Large-scale plasma was created in molecular gases ($O_2$, $N_2$, $C_2H_4$) and their mixtures by high-power laser-induced dielectric breakdown (LIDB). Compositions of the mixtures used are those suggested for the early Earth's atmosphere. Time-integrated as well as time-resolved optical emission spectra emitted from the laser spark have been measured and analyzed. The spectra of the plasma generated in the above mixtures are dominated by emission of diatomic radicals which are precursors of stable products as acetylene and hydrogen cyanide. Occurrence of these species was confirmed in irradiated gaseous mixture by FTIR spectroscopy. The figures below illustrate spectra of some hydrides formed in reactions due to discharge in different hydrogen-containing mixtures.

Baskakov et al. (2005) applied the Fourier transform spectroscopy to study a dc glow discharge in a mixture of argon and hydrogen. Several strong emission bands of $^{40}$ArH were observed in the 2500–8500 cm$^{-1}$ region. Rotational-electronic transitions of the two previously unstudied $4p$–$5s$ and $5p$–$6s$ ($v = 0$–$0$) bands of ArH were measured and assigned in the 6060 and 3770 cm$^{-1}$ regions, respectively. An overview spectrum of the $4p$–$5s$ and $5p$–$6s$ band is shown in Figure 16. There are still many unassigned bands in the observed spectra including higher vibrationally excited $v$–$v$ bands.

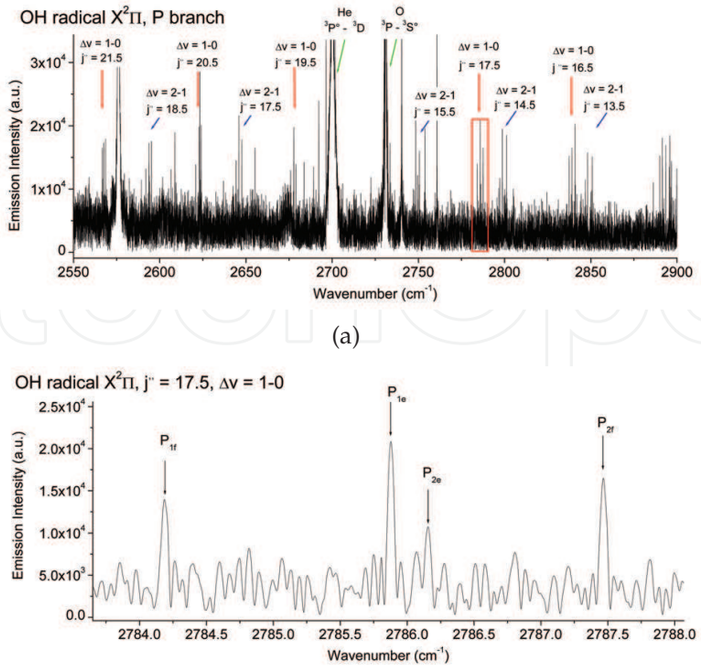


Fig. 12. Spectra of OH radical formed in $H_2 + O_2 + He$ mixture discharge

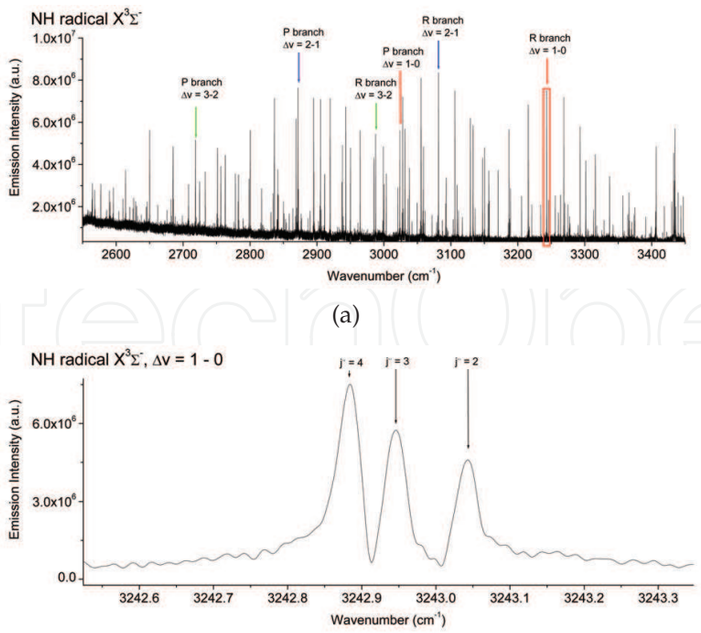


Fig. 13. Spectra of NH radical formed in $H_2 + N_2 + He$ mixture discharge

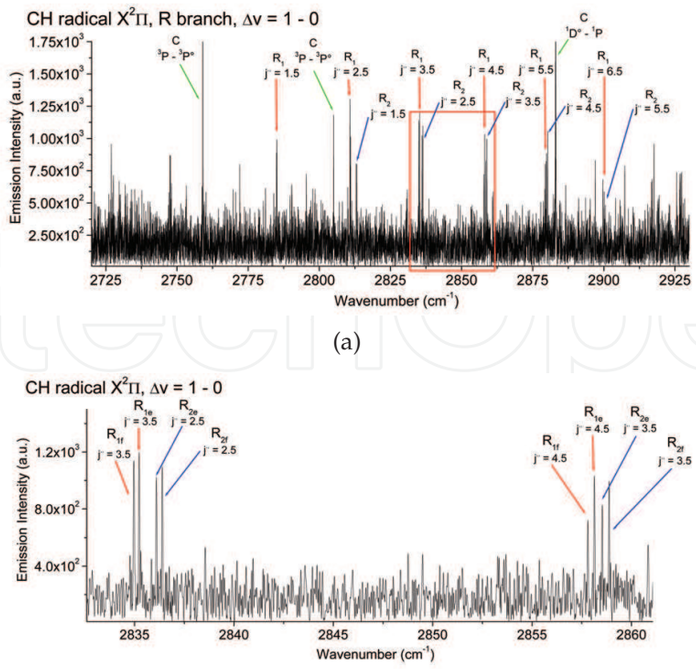


(a)

(b)

Fig. 14. Spectra of CH radical formed in $CH_4$ + He mixture discharge

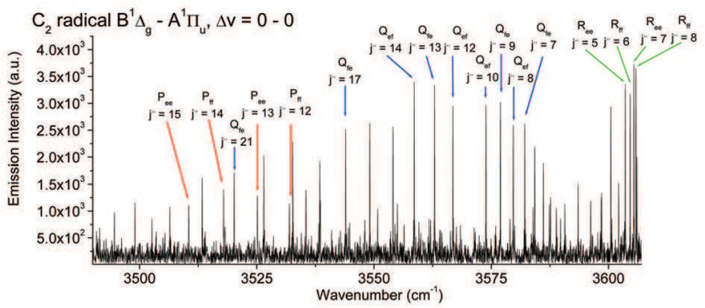


Fig. 15. Spectra of $C_2$ radical formed in $CH_4$ + He mixture discharge

## 3. Continuous scan systems: application with lasers

### 3.1 Interleaved sampling $1/n$

In the case of the measurement of time-resolved spectra in combination with a laser whose maximum repetition rate is slower than the interferometer mirror speed, there is no possibility of sampling at each individual trigger point of the He–Ne laser.

The lowest scanning speed of the interferometer is limited to the He–Ne laser fringe frequency of about 3 kHz. However, by utilizing the under-sampling condition, sampling several times more slowly becomes possible. Figure 17 shows the clock pattern for sampling in the present experiments where triggers for the pulse event and for the sampling are produced with a period of $1/n$ times the He–Ne laser fringe frequency. Complete interferograms are then obtained with $n$ scans if the trigger point is changed for each scan. The time sequence shown in Figure 17 corresponds to the case of $n = 3$.

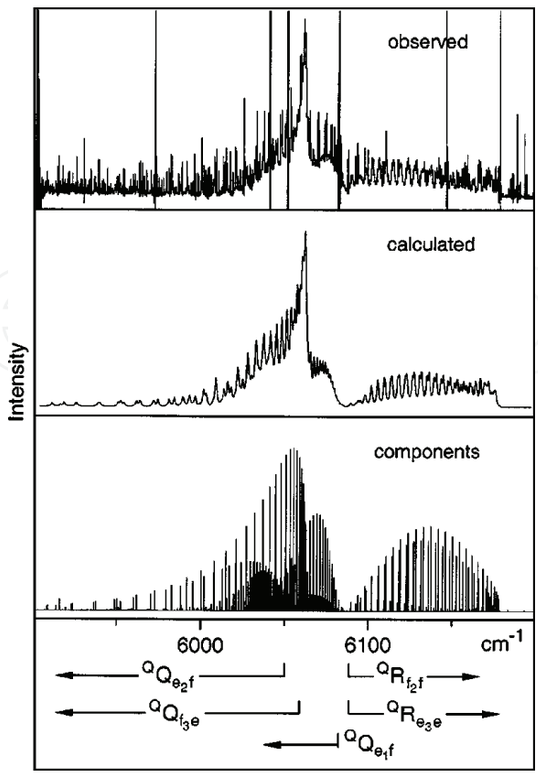


Fig. 16. Observed and calculated emission spectrum of the $4p$–$5s$ band of ArH. The strongest lines in the upper drawing originated from the Ar atom. Sharp lines belong to the $4f$–$3d$ band and probably to other unnassigned bands of ArH.

The maximum frequency of the used ArF laser is 1 kHz. The laser pulse is therefore repeated every 1000 $\mu$s. The minimum speed of the interferometer mirror is 3 kHz, then the digital signal produced by the He–Ne laser is repeated every 333.33 $\mu$s. In order to obtain data in the maximum density, *i. e.* for every trajectory difference defined by the He–Ne laser, the complete record is taken during three scans (for the mirror speed 3 kHz and laser repetition frequency 1 kHz). The complete set of the time-resolved spectra (one complete interferogram) is acquired by three time-shifted scans.

### 3.2 Synchronous triggering and data sampling

FT data are taken at the zero crossing points of the He–Ne laser fringe signals, while the wavelength of the He–Ne laser is used for the measurement of path differences. The data are sampled at time intervals which correspond to a mirror movement of either one wavelength or half a wavelength, depending on the frequency range of the measurements (8000 or 16000 $cm^{-1}$). Time resolved spectra are obtained by collecting data at various points between the zero-crossings and calculating the FT transformation for each such point. This system was utilized using a Field Programmable Gate Array processor (FPGA). The main role of the FPGA processor in our experiment was to create a discharge or laser pulse and AD trigger signals (the signal for data collection from the detector) synchronously with the He–Ne laser fringe signals from the spectrometer. The FPGA processor also controls the data transmission from the digital input board to the PC.

Figure 17 depicts the timing chart (clock pattern) produced by the FPGA for the laser-pulse ablation method. The scan signal and He–Ne laser fringe signals are supplied by the Bruker 120 HR spectrometer and used as the system time standard. A discharge trigger pulse is produced at a width which is preset by the FPGA. AD triggers are also produced by the FPGA with a time offset value between the beginning of the laser pulse and the interval between pulses. In the present experiments we used a 60 $\mu$s offset and interval values covering, 30 $\mu$s when 30 AD triggers were supplied. A series of data signals corresponding to the AD triggers are stored and Fourier-transformed.

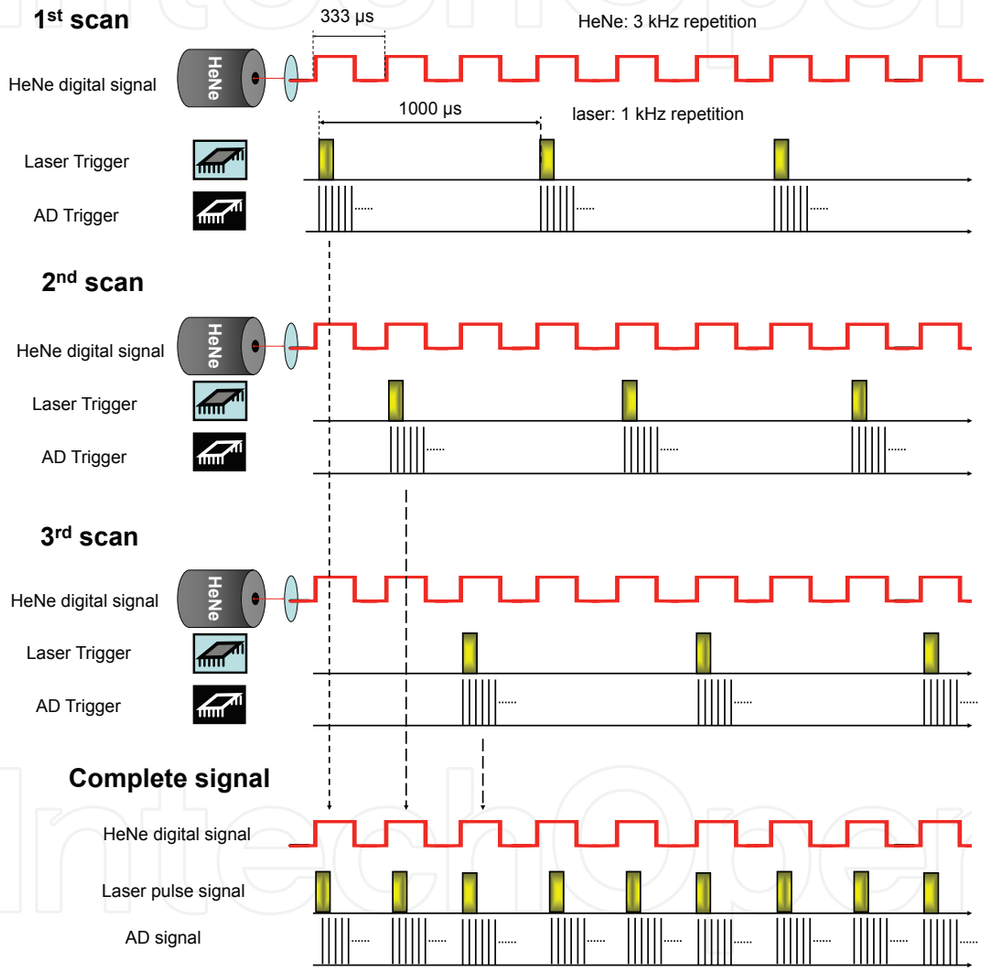


Fig. 17. Timing diagram for the interleaved sampling. During the scan, the laser pulse and the AD trigger sampling are induced with a rate of $1/n$ times of the He–Ne laser fringe frequency. The complete interferograms are obtained after $n$ scans ($n = 3$ here).

The maximum number of spectra taken by this method is 64. The time resolution is about 1 $\mu$s, which is limited by the band width of the detector amplifier. The present system collects 64 times more data in comparison to the original Bruker system. This is possible because of rapid development in the field of PCs, their memory size and the writing speed of the hard

disk. In the case of our current data collection program, we are able to store 64 interferograms in a single scan when the resolution is up to 0.03 $cm^{-1}$. For resolutions higher than 0.03 $cm^{-1}$, 30 time-resolved data are recorded simultaneously, which means the number of time-resolved data points can be varied according to the type of experiment and the memory capacity.

### 3.3 The experimental setup

The time resolution FTIR spectra were measured using the modified Bruker IFS 120 HR spectrometer (modified for the time-resolution scan of emission data) in a spectral range of 1800–6000 $cm^{-1}$ using a $CaF_2$ beam splitter,and an InSb detector. The aperture size was 4 mm, the preamplifier gain was 3. The spectra were measured at a resolution of 0.1 $cm^{-1}$ with a MID IR filter for the range of 1538–3500 $cm^{-1}$ (number of scans from 1 to 10, zero filling 2, trapezoid apodization function).

The Bruker system was equipped with an analog-digital converter (ADC 4322: Analogic, USA), which was connected to a PC containing a programmable control processor of Field Programmable Gate Array – FPGA, (ACEX 1K: Altera, USA) set up at a frequency of 33 MHz, and digital input board PCI (2172C: Interface, Japan). The data collection process and synchronization with the laser were controlled by the FPGA processor programmed by QUARTUS II 7.1, Altera. The computer programs for data acquisition and fast FT transformation and displaying of the data were written in $C^{++}$ language.

Time-resolved FTIR spectroscopy was applied for observations of the emission arising after the irradiation of metals with a pulsed nanosecond ArF ($\lambda = 193$ nm) laser. A high repetition rate ArF laser ExciStar S-Industrial V2.0 1000 (193 nm, laser pulse width 12 ns, frequency 1 kHz) with 15 mJ output power was focused on a rotating and linearly traversing gold target inside a vacuum chamber (average pressure $10^{-2}$ Torr). The infrared emission (axial distance from the target 10 mm) was focused into the spectrometer using a $CaF_2$ (100 mm) lens (see Figure 18). The emission was observed in the 1800–3500 $cm^{-1}$ spectral region with a time profile showing maximum emission intensity at 9–11 $\mu$s after the laser shot.

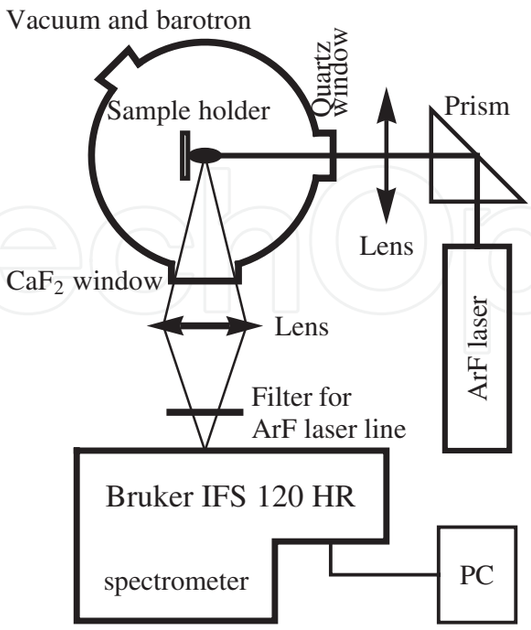


Fig. 18. Experimental set-up of the metal emission measurement.

For data sampling we used the so-called 1/3 sampling, where the scanner rate was set to produce a 3 kHz HeNe laser interference signal, the ArF laser oscillation was triggered, and 30 sets of time-resolved data were recorded with a preset time interval of 1 $\mu$s. Three scans were needed for a complete interferogram, and only 5 scans were coadded to improve the signal-to-noise ratio. The acquired spectra were post-zerofilled in the OPUS program and subsequently corrected by subtracting the blackbody background spectrum. The wavenumbers, line widths and their intensities were then obtained using the peak picking method (OPUS).

## 4. TR FTIR emission spectroscopy

### 4.1 Introduction

Pulsed laser ablation and depositing processes are currently frequently used techniques. Laser induced plasma at low fluence (typically 10 J/cm$^2$) has numerous applications, *e. g.* Pulsed Laser Deposition (PLD) or multi-elemental analysis. The latter technique, known as Laser Induced Plasma Spectroscopy (LIPS) or Laser-Induced Breakdown Spectroscopy (LIBS) consists of analyzing the light spectrum emitted from a plasma created on the sample surface by laser pulses. LIPS has many practical advantages over the conventional methods of chemical analysis of elements and is consequently being considered for a growing number of applications (Babánková et al., 2006; Barthélemy et al., 2005; Gomes et al., 2004; Lee et al., 2004; Radziemski & Cremers, 1989).

Excimer lasers operating in near-ultraviolet regions with typical laser fluences of 1–30 J/cm$^2$ are used for many types of ablation (Claeyssens et al., 2003). The ablation plume arising after irradiation with fluences of nanosecond duration pulses is governed by a great number of very complex physical processes. During the laser pulse (with typical duration of 20 ns), the laser photons heat the sample and bring a part of its surface to the critical temperature. The heated material starts to boil explosively (Miotello & Kelly, 1999) and creates an emission plume consisting of ejected particles, atoms and ions. The particles inside the plume can themselves interact with the laser photons, which leads to a subsequent rise in the temperature of the ablation plume and to photochemical and photodissociation processes (Rubahn, 1999, p. 219). The population of Rydberg states responsible for IR emission lines is governed mainly by collisional processes. The electrons created in the photodissociation processes can interact with the laser pulse via the electron-ion inverse bremsstrahlung, which again causes additional heating of the plume (Vertes et al., 1994) and leads to the fast transition of the plume from ionized gas to plasma. The electrons escaping from the corona region cause a separation of charges, thereby inducing the ionized part of the plasma to accelerate. After the end of the laser pulse, the plume expands adiabatically. The electron-ion collision inside the plume can create excited ions. The electron-ion collision in the presence of a third body can results in their recombination leading to formation of atoms in highly excited Rydberg states (Claeyssens et al., 2001). A radiative cascade of these Rydberg states is then observed as the optical emission of the ablation plume.

The investigation of such emission is complicated by nonequilibrium and nonstationary conditions of the plasma for the excited states (Aragon & Aguilera, 2008), so the information on population dynamics is only scarcely available for these states Rossa et al. (2009). As an example of such data we report temporal evolution dynamics for each IR atomic line of the recorded spectra of metal atoms.

The properties of the observed plumes obtained by the ablation of different materials can eventually reflect the superposition of the ensemble processes described above. Here we

report some results of a study focused on time-resolved spectra arising from 193 nm pulsed laser ablation of metallic (Au, Ag and Cu) targets in a $10^{-3}$ Torr vacuum. The atomic metal spectra were measured by a high resolution Fourier Transform infrared spectrometer specially modified for time-resolved measurements (Civiš et al., 2010; Civiš et al., 2010).

### 4.2 Results for Au

The observed IR emission spectra of the Au atom are presented in Figure 19 at 10 $\mu$s after the laser shot, when the time profile of the emission intensity is maximum for all the observed lines.

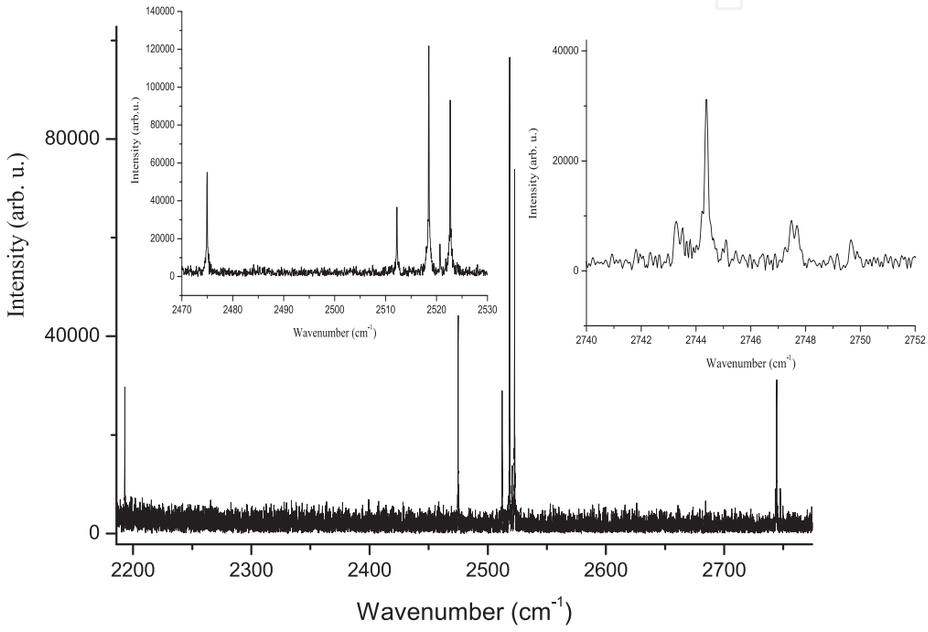


Fig. 19. Some parts of the observed IR emission spectra of Au. The 2743.358 $cm^{-1}$ and 2747.567 $cm^{-1}$ values are given to the centers of gravity of the hyperfine patterns clearly seen in the second graph as double peaks.

Although the Au spectrum has been studied in various spectral domains for several decades (Brown & Ginter, 1978; Ding et al., 1989; Dyubko et al., 2005; Ehrhardt & Davis, 1971; George et al., 1988; Jannitti et al., 1979; Platt & Sawyer, 1941), to our knowledge only one experimental study George et al. (1988) concerning the studied 3–5 $\mu$m IR range is reported. As compared to George et al. (1988) we observed several strong new Au lines in the 1800–4000 $cm^{-1}$ domain. The most prominent IR lines observed for Au are listed in Table 3. Their half-widths at half-maxima (HWHM) are calculated from fitting to the Lorentzian shape. The decay time, $\tau$ given in the Table 3 was calculated by fitting of the measured time profiles of the corresponding lines. These profiles are given in Figure 20. The time decay of most of the strong lines is well described by exponential fitting, excepting the 2156.484 $cm^{-1}$ line which demonstrates a non-constant decay rate during the 30 $\mu$s after the laser shot. Some weaker lines demonstrate such behavior more clearly, their decay is not exponential (and is

| Wavenumber ($cm^{-1}$) | Intensity (arb.u) | HWHM ($cm^{-1}$) | Decay time ($\mu$s) | Identification |
|---|---|---|---|---|
| 2156.484 | 12679 | 0.098 | $5.24 \pm 1.7^*$ | $8f_{\frac{7}{2}} \rightarrow 8d_{\frac{5}{2}}$ |
| 2193.030 | 38690 | 0.12 | $6.56 \pm 0.61$ | $8s_{\frac{1}{2}} \rightarrow 8p_{\frac{1}{2}}$ |
| 2428.358 | 8024 | 0.39 | $6.36 \pm 1.4^*$ | $12s_{\frac{1}{2}} \rightarrow 9p_{\frac{3}{2}}$ |
| 2474.954 | 53951 | 0.13 | $5.25 \pm 0.21$ | $7d_{\frac{5}{2}} \rightarrow 6f_{\frac{7}{2}}$ |
| 2512.219 | 36631 | 0.14 | $5.73 \pm 0.25$ | $9p_{\frac{1}{2}} \rightarrow 10d_{\frac{3}{2}}$ |
| 2518.489 | 121588 | 0.13 | $5.56 \pm 0.22$ | $7d_{\frac{3}{2}} \rightarrow 6f_{\frac{5}{2}}$ |
| 2520.684 | 16574 | 0.16 | $6.83 \pm 0.58$ | $8p_{\frac{3}{2}} \rightarrow 8d_{\frac{5}{2}}$ |
| 2522.683 | 91622 | 0.13 | $5.70 \pm 0.36$ | $5f_{\frac{7}{2}} \rightarrow 8d_{\frac{5}{2}}$ |
| 2743.370 | 8780 | 0.39 | $5.41 \pm 1.2^*$ | ? |
| 2744.380 | 41786 | 0.12 | $5.96 \pm 0.68$ | $8s_{\frac{1}{2}} \rightarrow 8p_{\frac{3}{2}}$ |
| 2747.567 | 10249 | 0.13 | $8.52 \pm 2.6^*$ | $12s_{\frac{1}{2}} \rightarrow 9p_{\frac{1}{2}}$ |
| 2749.6 | 6453 | 0.27 | $5.51 \pm 1.8^*$ | $23p_{\frac{1}{2},\frac{3}{2}} \rightarrow 9d_{\frac{3}{2}}$ |
| 3187.811 | 13199 | 0.093 | $6.03 \pm 0.91^*$ | $(5d^9 6s)6p_{\frac{3}{2}} \rightarrow 6d_{\frac{5}{2}}$ |
| 3828.96 | 9540 | 0.14 | $5.47 \pm 2.0^*$ | $7f_{\frac{7}{2}} \rightarrow 7d_{\frac{5}{2}}$ |
| 3862.41 | 9370 | 0.13 | $2.98 \pm 1.1^*$ | $9d_{\frac{3}{2}} \rightarrow 5f_{\frac{5}{2}}$ |
| 3866.606 | 7738 | 0.11 | $6.84 \pm 0.83^*$ | $9d_{\frac{3}{2}} \rightarrow 8p_{\frac{3}{2}}$ |

Table 3. Experimental Au lines and their identification. The decay time, $\tau$, was calculated by exponential fitting of the measured time profiles of the corresponding lines. Time profile of the lines denoted by asterisk demonstrates significant deviation from the exponential decay; $\tau$ values are roughly approximate

even non-monotonic), so their $\tau$ values are estimated in Table 3 in a rough approximation. Such a non-monotonic decay can be due to more complex population kinetics of the atomic Au states in the ablation plasma. We consider most of the observed lines to be due to transitions between the Rydberg $n = 5..10$ states of the valence electron outside the closed-shell $5d^{10}$ core.

### 4.3 Results for Ag

Some parts of the observed IR emission spectra of the Ag atom are presented in Figure 21 at 11 $\mu$s after the laser shot, when the time profile of the emission intensity is maximum for all the observed lines. The most prominent IR lines observed for Ag are listed in Table 4. Their full widths at half-maxima (FWHM) are calculated from fitting to a Voigt profile, but under our conditions this profile does not differ much from the Lorentzian shape (see Ref. Civiš et al. (2010)).

We measured the emission spectrum at a different delay time, from 0 to 30 $\mu$s, after the laser shot. This allows us to measure the time profiles of the observed Ag lines. Some such profiles are shown in Figure 22. The temporal decay of some lines is well described by exponential fitting, while some lines display non-exponential (including some "plateaux" at 20–25 $\mu$s after the laser shot) and even non-monotonic behavior. Therefore their decay time, $\tau$, values are estimated in Table 4 in a rough approximation; so, for essentially non-exponential decays, the standard deviation $\Delta\tau$ is of order of $\tau$.

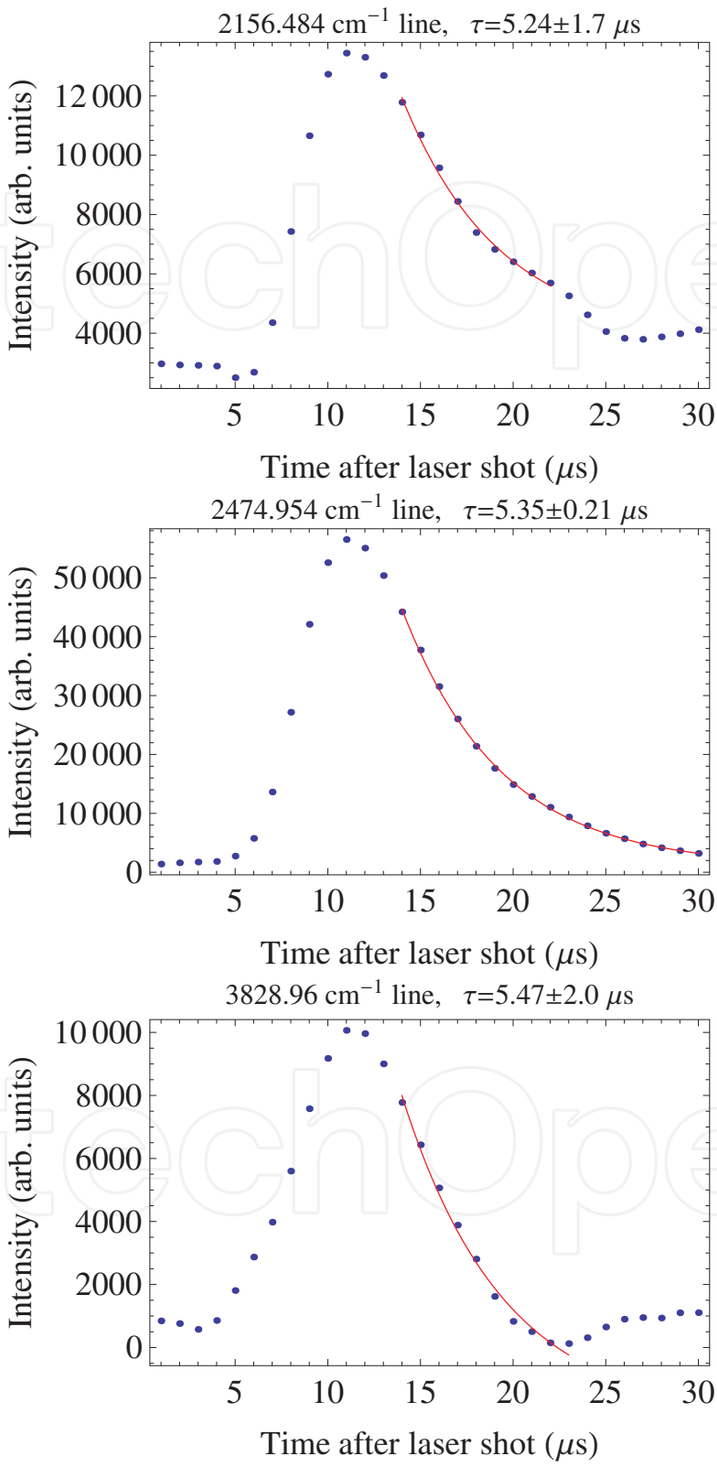


Fig. 20. The time profiles of some observed lines (dots) and their fit with exponential decay (solid curves)

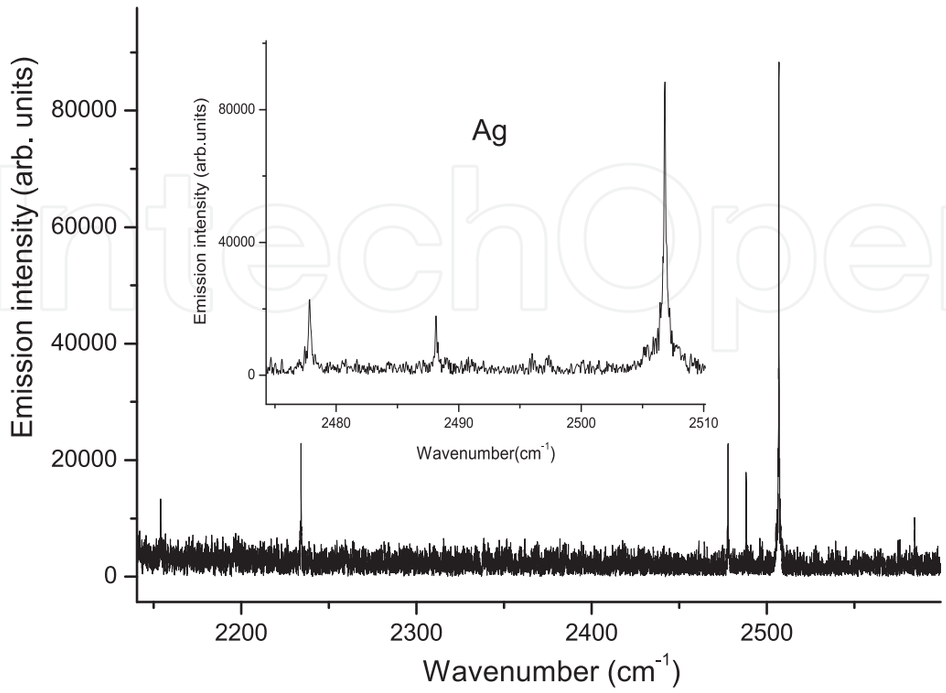


Fig. 21. A section of the the observed IR emission spectra of Ag.

It should be noted that the decay times $\tau \simeq$ 1–10 $\mu$s given in Table 4 are not related to the radiative lifetimes of Ag atom levels which are at least two orders shorter (Bengtsson et al., 1991; 1990; Zhankui et al., 1990). The temporal dynamics shown in Figure 22 is due to a complex combination of the collisional cascade repopulation of the emitting levels (Civiš et al., 2010) and the transfer processes in ablation products (Kawaguchi et al., 2008).
The revised energy values $E_i$ of some Ag terms are presented in Table 5. For the levels with $n \leq 6$ our values coincides with the reference values within the uncertainty intervals, but it is not the case for $n > 6$. However we consider our values preferable since they are extracted from spectra recorded with 0.02 cm$^{-1}$ resolution while the reference values were obtained from spectra with resolution of 0.035–0.045 cm$^{-1}$ Pickering & Zilio (2001) and 0.06 cm$^{-1}$ Brown & Ginter (1977)

### 4.4 Results for Cu

Figure 23 shows some parts of the observed IR emission spectra of Cu I at 20 $\mu$s after the laser shot, when the emission intensity is maximal for almost all of the observed lines. The list of the IR lines observed for Cu I is presented in Table 6. Their full widths at half-maxima (FWHM) are calculated from fitting to the Lorentzian shape (Civiš et al., 2010; Civiš et al., 2010).
As in the cases of Au and ag, we measured the time profiles of the observed Cu lines, *i. e.* their emission intensities as functions of the delay time, from 0 to 60 $\mu$s, after the laser shot. Some such profiles are shown in Figure 24. While the temporal decay of some lines can be fitted, at least roughly, by an exponential function, several lines display essentially non-exponential behavior including some "plateaux" or even secondary maxima at 35–50 $\mu$s after the laser

| Wavenumber ($cm^{-1}$) | Intensity (arb. units) | SNR | FWHM ($cm^{-1}$) | Decay time ($\mu$s) | Identification |
|---|---|---|---|---|---|
| 1345.570(6) | 14889 | 14. | 0.125(55) | 4.17(104)(*b*) | $(4d^{10})7d_{\frac{3}{2}} \leftarrow (4d^{10})6f_{\frac{5}{2}}$ |
| 1363.326(14) | 3910 | 4.3 | 0.146(150) | 5.90(609)(*b*) | $(4d^{10})5f \leftarrow (4d^{10})6g$ |
| 1460.115(6) | 4530 | 5.6 | 0.111(035) | 3.34(170)(*b*) | $(4d^{10})7p_{\frac{3}{2}} \leftarrow (4d^{10})8s_{\frac{1}{2}}$ |
| 2149.320(2) | 6956 | 2.4 | 0.025(19) | 7.17(206)(*b*) | $(4d^{10})7d_{\frac{5}{2}} \leftarrow (4d^{10})7f_{\frac{7}{2}}$ |
| 2153.988(4) | 32525 | 9.4 | 0.031(21) | 3.07(15) | $(4d^{10})7s_{\frac{1}{2}} \leftarrow (4d^{10})7p_{\frac{1}{2}}$ |
| 2154.599(2) | 5958 | 2.2 | 0.029(11) | 12.8(78)(*b*) | $(4d^{10})7d_{\frac{3}{2}} \leftarrow (4d^{10})7f_{\frac{5}{2}}$ |
| 2234.168(1) | 74835 | 13. | 0.035(6) | 3.63(34) | $(4d^{10})7s_{\frac{1}{2}} \leftarrow (4d^{10})7p_{\frac{3}{2}}$ |
| 2417.757(2) | 4880 | 5.9 | 0.030(14) | 5.03(214)(*b*) | $(4d^{10})6d_{\frac{3}{2}} \leftarrow (4d^{10})8p_{\frac{1}{2}}$ |
| 2447.045(2) | 5463 | 6.6 | 0.026(24) | 4.88(81)(*b*) | $(4d^{10})6d_{\frac{5}{2}} \leftarrow (4d^{10})8p_{\frac{3}{2}}$ |
| 2477.833(1) | 113278 | 10. | 0.044(4) | 4.27(29) | $(4d^{10})6d_{\frac{5}{2}} \leftarrow (4d^{10})5f_{\frac{7}{2}}$ |
| 2488.1560(9) | 78947 | 7.0 | 0.048(4) | 4.20(35)(*a*) | $(4d^{10})6d_{\frac{3}{2}} \leftarrow (4d^{10})5f_{\frac{5}{2}}$ |
| 2506.8196(5) | 460526 | 41. | 0.056(2) | 3.87(20) | $(4d^{10})4f \leftarrow (4d^{10})5g$ |
| 2579.210(3) | 5252 | 6.2 | 0.036(21) | 5.14(202)(*b*) | $(4d^{10})7p_{\frac{3}{2}} \leftarrow (4d^{10})7d_{\frac{3}{2}}$ |
| 2584.3387(6) | 48450 | 31. | 0.041(3) | 4.20(37)(*b*) | $(4d^{10})7p_{\frac{3}{2}} \leftarrow (4d^{10})7d_{\frac{5}{2}}$ |
| 2658.7911(9) | 22693 | 14. | 0.038(5) | 4.15(39)(*a*) | $(4d^{10})7p_{\frac{1}{2}} \leftarrow (4d^{10})7d_{\frac{3}{2}}$ |
| 3386.152(1) | 98370 | 9.2 | 0.059(6) | 3.35(28) | $(4d^{10})6p_{\frac{3}{2}} \leftarrow (4d^{10})7s_{\frac{1}{2}}$ |
| 3589.552(5) | 13825 | 15. | 0.065(4) | 3.15(11)(*a*) | $(4d^{10})6p_{\frac{1}{2}} \leftarrow (4d^{10})7s_{\frac{1}{2}}$ |

Table 4. Experimental Ag lines and their identification. The decay time, $\tau$, was calculated by exponential fitting of the measured time profiles of the corresponding lines. The profiles denoted as ((a)) demonstrates significant deviation from the exponential decay; those denoted by (b) demonstrate the decay curves of essentially non-exponential form with a plateau or a second maximum; $\tau$ value is roughly approximate

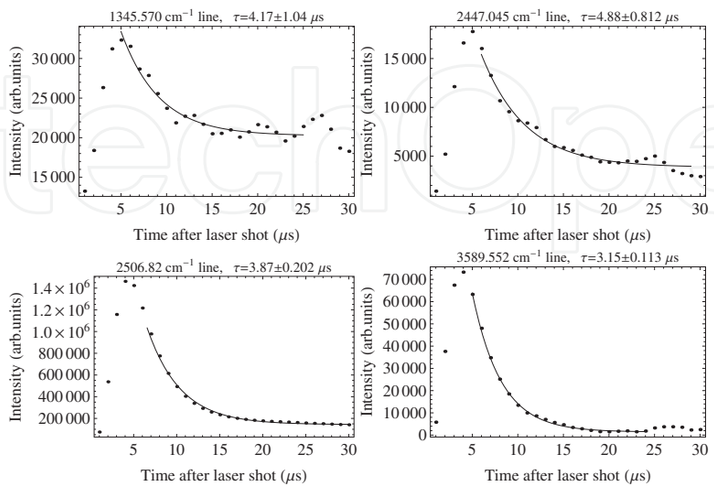


Fig. 22. The time profiles of some observed Ag lines (dots) and their fit with exponential decay (solid curves)

| Term | Energy ($cm^{-1}$) | Other sources |
|---|---|---|
| $(4d^{10})5f_{\frac{5}{2}}$ | 56691.275(2) | 56691.4 Shenstone (1940), 56692.5 Safronova et al. (2003) |
| $(4d^{10})5f_{\frac{7}{2}}$ | 56691.397(4) | 56691.4 Shenstone (1940), 56694.4 Safronova et al. (2003) |
| $(4d^{10})6p_{\frac{1}{2}}$ | 48297.402(2) | 48297.402(3) Pickering & Zilio (2001) |
| $(4d^{10})6p_{\frac{3}{2}}$ | 48500.804(1) | 48500.804(2) Pickering & Zilio (2001) |
| $(4d^{10})6d_{\frac{3}{2}}$ | 54203.119(2) | 54203.119(2) Pickering & Zilio (2001) |
| $(4d^{10})6d_{\frac{5}{2}}$ | 54213.564(3) | 54213.570(3) Pickering & Zilio (2001) |
| $(4d^{10})6f_{\frac{5}{2}}$ | 58045.481(7) | This work |
| $(4d^{10})6g$ | 58054.723(16) | This work |
| $(4d^{10})7s_{\frac{1}{2}}$ | 51886.954(1) | 51886.971(2) Pickering & Zilio (2001) |
| $(4d^{10})7p_{\frac{1}{2}}$ | 54041.087(2) | 54040.99(6) Brown & Ginter (1977) |
| $(4d^{10})7p_{\frac{3}{2}}$ | 54121.059(2) | 54121.129(5) Pickering & Zilio (2001) |
| $(4d^{10})8s_{\frac{1}{2}}$ | 55581.246(3) | 55581.258(3) Pickering & Zilio (2001) |
| $(4d^{10})8p_{\frac{1}{2}}$ | 56620.876(3) | 56620.72(6) Brown & Ginter (1977) |
| $(4d^{10})8p_{\frac{3}{2}}$ | 56660.596(6) | 56660.559(17) Pickering & Zilio (2001) |
| $(4d^{10})7d_{\frac{3}{2}}$ | 56699.911(2) | 56699.768(3) Pickering & Zilio (2001) |
| $(4d^{10})7d_{\frac{5}{2}}$ | 56705.435(2) | 56705.498(3) Pickering & Zilio (2001) |
| $(4d^{10})7f_{\frac{5}{2}}$ | 58854.510(3) | This work |
| $(4d^{10})7f_{\frac{7}{2}}$ | 58854.755(3) | This work |

Table 5. Revised values of some levels of Ag I

shot. Their decay time, $\tau$, values are therefore estimated in Table 6 in a rough approximation; it is seen from this table that for essentially non-exponential decays the uncertainity $\Delta\tau$ is of the same order of magnitude as $\tau$ itself. Note that that the decay times $\tau$ given in Table 6 are due to a complex combination of the collisional cascade repopulation of the emitting levels (Civiš et al., 2010) and the transfer processes in ablation products (Kawaguchi et al., 2008) and by no means related to the radiative lifetimes of the atomic levels. The temporal dynamics of some lines is shown in Figure 24.

After the assignment we refined the energy values for some levels involved into the classified transitions; the revised values of these energies are presented in Table 7. It is interesting to note that the fine-structure $5p$ doublet (fine splitting is about 0.3 $cm^{-1}$) is well resolved in our experiment unlike the previous measurements Longmire et al. (1980); Shenstone (1948) where only a single line was observed. The ratio of the $5p_{\frac{3}{2}} \leftarrow 6s_{\frac{1}{2}}$ and $5p_{\frac{1}{2}} \leftarrow 6s_{\frac{1}{2}}$ transition intensities is close to theoretical nonrelativistic value 2:1.

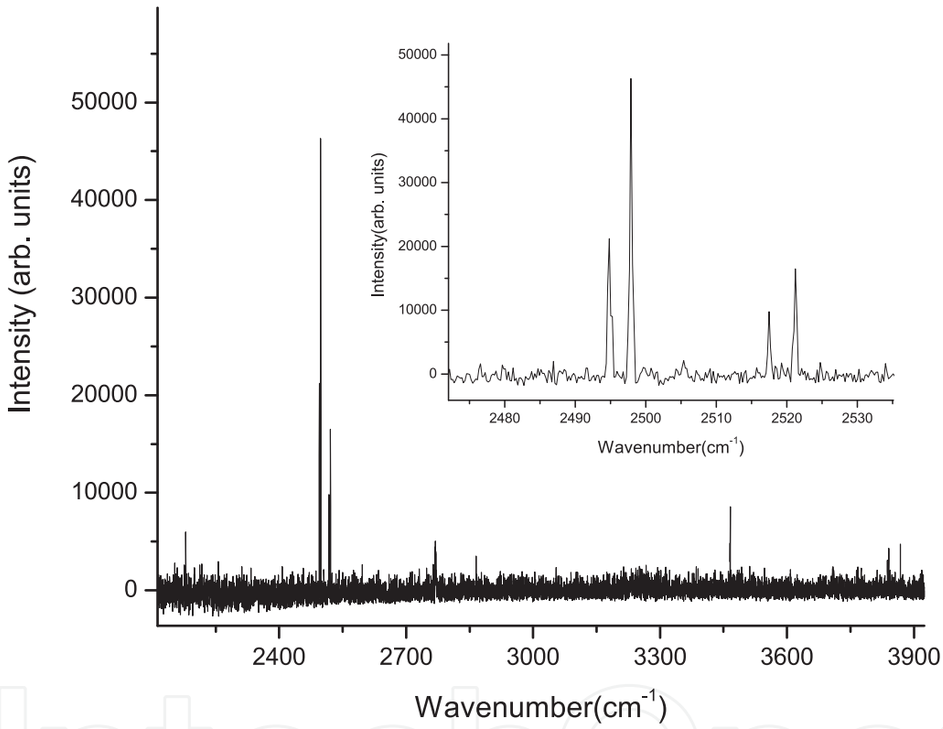


Fig. 23. Some parts of the observed IR emission spectra of Cu I

| Wavenumber ($cm^{-1}$) | Intensity (arb. units) | SNR | FWHM ($cm^{-1}$) | Decay time ($\mu$s) | Identification |
|---|---|---|---|---|---|
| 1887.307(6) | $1.30 \times 10^4$ | 17. | 0.083(16) | 12.1(44) (b) | $6p_{\frac{3}{2}} \leftarrow 7s_{\frac{1}{2}}$ |
| 1935.313(2) | $6.58 \times 10^4$ | 63. | 0.106(5) | 5.88(221) (b) | $6s_{\frac{1}{2}} \leftarrow 6p_{\frac{3}{2}}$ |
| 2163.890(16) | $3.42 \times 10^2$ | 6.2 | 0.104(46) | 16.2(41) (a) | $5f_{\frac{7}{2}} \leftarrow 7g_{\frac{9}{2}}$ |
| 2171.118(18) | $1.64 \times 10^2$ | 4.6 | 0.074(55) | 9.50(266) (a) | $5f_{\frac{5}{2}} \leftarrow 7g_{\frac{7}{2}}$ |
| 2176.426(16) | $2.16 \times 10^2$ | 5.6 | 0.077(43) | 12.8(34) (b) | $6d_{\frac{5}{2}} \leftarrow 7f_{\frac{7}{2}}$ |
| 2179.011(3) | $7.68 \times 10^4$ | 58. | 0.065(10) | 9.06(479) (a) | $6s_{\frac{1}{2}} \leftarrow 6p_{\frac{1}{2}}$ |
| 2494.8098(3) | $2.98 \times 10^5$ | 63. | 0.038(1) | 11.7(42) (b) | $4f_{\frac{5}{2}} \leftarrow 5g_{\frac{7}{2}}$ |
| 2497.7750(3) | $3.77 \times 10^5$ | 121. | 0.041(1) | 11.3(36) (b) | $4f_{\frac{7}{2}} \leftarrow 5g_{\frac{9}{2}}$ |
| 2513.814(4) | $4.65 \times 10^3$ | 8.4 | 0.048(13) | 11.5(41) (b) | $5d_{\frac{5}{2}} \leftarrow 5f_{\frac{5}{2}}$ |
| 2517.4511(3) | $1.03 \times 10^5$ | 78. | 0.051(1) | 15.0(57) (b) | $5d_{\frac{3}{2}} \leftarrow 5f_{\frac{5}{2}}$ |
| 2521.0550(3) | $1.58 \times 10^5$ | 129. | 0.049(1) | 14.9(57) (b) | $5d_{\frac{5}{2}} \leftarrow 5f_{\frac{7}{2}}$ |
| 2865.233(2) | $2.32 \times 10^4$ | 37. | 0.062(5) | 7.93(167) (b) | $6p_{\frac{1}{2}} \leftarrow 6d_{\frac{3}{2}}$ |
| 3110.955(4) | $2.06 \times 10^4$ | 27 | 0.087(11) | 8.53(214) (b) | $6p_{\frac{3}{2}} \leftarrow 6d_{\frac{5}{2}}$ |
| 3465.481(4) | $8.46 \times 10^4$ | 10. | 0.089(13) | 5.06(87) (b) | $5p_{\frac{1}{2}} \leftarrow 6s_{\frac{1}{2}}$ |
| 3465.8044(7) | $1.70 \times 10^5$ | 23. | 0.048(2) | 5.25(90) (b) | $5p_{\frac{3}{2}} \leftarrow 6s_{\frac{1}{2}}$ |
| 3837.402(12) | $7.49 \times 10^3$ | 9.5 | 0.193(36) | 8.51(209) (a) | $4f_{\frac{5}{2}} \leftarrow 6g_{\frac{7}{2}}$ |
| 3840.376(15) | $9.64 \times 10^3$ | 11. | 0.235(47) | 14.7(190) (a) | $4f_{\frac{7}{2}} \leftarrow 6g_{\frac{9}{2}}$ |

Table 6. Experimental Cu I lines and their identification. The decay time, $\tau$, was calculated by exponential fitting of the measured time profiles of the corresponding lines. See the caption to Table 4

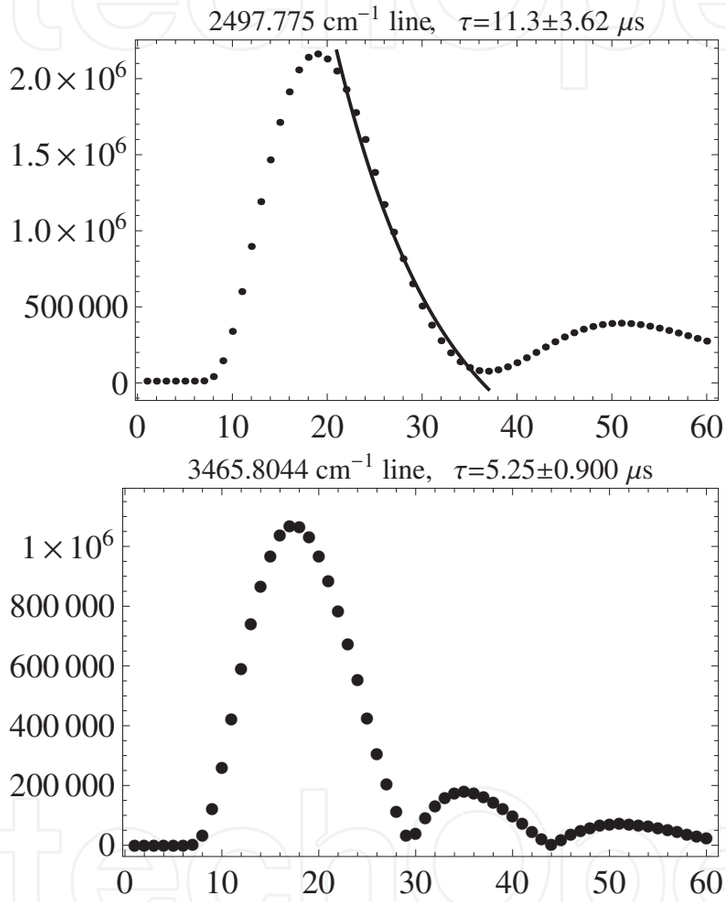


Fig. 24. The time profiles of some observed Cu I lines (dots) and their fit with exponential decay (solid curves)

| Term | Energy ($cm^{-1}$) | Other sources |
|---|---|---|
| $(3d^{10})5p_{\frac{1}{2}}$ | 49383.263(23) | 49383.26 Shenstone (1948) |
| $(3d^{10})5p_{\frac{3}{2}}$ | 49382.949(14) | 49382.95 Shenstone (1948) |
| $(3d^{10})5d_{\frac{3}{2}}$ | 55387.621(11) | 55387.668 Shenstone (1948) |
| $(3d^{10})5d_{\frac{5}{2}}$ | 55390.569(9) | 55391.292 Shenstone (1948) |
| $(3d^{10})5f_{\frac{5}{2}}$ | 57905.041(14) | 57905.2 Shenstone (1948), 57905.23 Longmire et al. (1980) |
| $(3d^{10})5f_{\frac{7}{2}}$ | 57911.090(12) | 57908.7 Shenstone (1948) |
| $(3d^{10})5g_{\frac{7}{2}}$ | 57924.610(30) | This work |
| $(3d^{10})5g_{\frac{9}{2}}$ | 57924.075(30) | This work |
| $(3d^{10})6s_{\frac{1}{2}}$ | 52848.752(9) | 52848.749 Shenstone (1948) |
| $(3d^{10})6p_{\frac{1}{2}}$ | 55027.763(26) | 55027.74 Shenstone (1948), 55027.713 Longmire et al. (1980) |
| $(3d^{10})6p_{\frac{3}{2}}$ | 54784.081(21) | 54784.06 Shenstone (1948), 54784.073 Longmire et al. (1980) |
| $(3d^{10})6d_{\frac{3}{2}}$ | 57893.028(24) | 57893.05 Shenstone (1948) |
| $(3d^{10})6d_{\frac{5}{2}}$ | 57895.084(24) | 57895.1 Shenstone (1948) |
| $(3d^{10})6g_{\frac{7}{2}}$ | 57267.202(33) | This work |
| $(3d^{10})6g_{\frac{9}{2}}$ | 57266.676(34) | This work |
| $(3d^{10})7f_{\frac{7}{2}}$ | 60071.510(30) | This work |
| $(3d^{10})7g_{\frac{7}{2}}$ | 60076.159(23) | This work |
| $(3d^{10})7g_{\frac{9}{2}}$ | 60074.980(20) | This work |

Table 7. Revised values of some levels of Cu I

## 5. Conclusion

The longstanding interests of our laboratory are the spectroscopic investigations of molecular ions, radicals or atoms which play a fundamental role in many plasma chemical processes, as well as in the reactions taking place inside of interstellar clouds or in stellar envelopes of giant stars of our universe.
The presented report is focused on the development and application of a time resolved system based on commercially available continuously scanning high resolution interferometer and its modification for time resolved Fourier transform spectroscopy.
The use of time-resolved FT spectroscopy opens new pathways and new points of view in study of the formation and decay processes inside the discharge or laser plasma.
Here, we are able to study the individual processes using atomic or molecular lines in a very wide spectral range of the high resolution FT technology, which has been simultaneously extended into the time dimension.
The only limitation is the sensitivity of the infrared FT technique, together with the considerable time required for the acquisition of the spectral data.

## 6. References

Aragon, C. & Aguilera, J. A. (2008). Characterization of laser induced plasmas by optical emission spectroscopy: A review of experiments and methods, *Spectrochim. Acta, Part B* **63**(9): 893–916.

Babánková, D., Civiš, S. & Juha, L. (2006). Chemical consequences of laser-induced breakdown in molecular gases, *Progress in Quantum Electronics* **30**(2-3): 75 – 88.

Barthélemy, O., Margot, J., Chaker, M., Sabsabi, M., Vidal, F., Johnston, T. W., Laville, S. & Drogoff, B. L. (2005). Influence of the laser parameters on the space and time characteristics of an aluminum laser-induced plasma, *Spectrochim. Acta, Part B* **60**(7-8): 905 – 914. 3rd International Conference on Laser Induced Plasma Spectroscopy and Applications (LIBS04), Torremolinos, SPAIN, SEP 28-OCT 01, 2004.

Baskakov, O. I., Civiš, S. & Kawaguchi, K. (2005). High resolution emission fourier transform infrared spectra of the 4p-5s and 5p-6s bands of arh, *The Journal of Chemical Physics* **122**(11): 114314.

Bengtsson, G. J., Jönsson, P., Larsson, J. & Svanberg, S. (1991). Time-resolved spectroscopic studies of the $7p\ ^2P$ states of neutral silver following vuv excitation, *ZPD* **22**(1): 437–439.

Bengtsson, J., Larsson, J. & Svanberg, S. (1990). Hyperfine structure and radiative-lifetime determination for the $4d^{10}6p\ ^2P$ states of neutral silver using pulsed laser spectroscopy, *Phys. Rev. A* **42**(9): 5457–5463.

Berg, P. A. & Sloan, J. J. (1993). Compact standalone data acquisition system for submicrosecond time-resolved fourier transform spectroscopy, *Rev. Sci. Instrum.* **64**(9): 2508–2514.

Bernath, P. F. & McLeod, S. (2001). DiRef, a database of references associated with the spectra of diatomic molecules, *J. Mol. Spectrosc.* **207**(2): 287.

Brown, C. M. & Ginter, M. L. (1977). Absorption spectrum of Ag I between 1540 and 1850 Å, *J. Opt. Soc. Am.* **67**(10): 1323–1327.

Brown, C. M. & Ginter, M. L. (1978). Absorption spectrum of Au I between 1300 and 1900 Å, *J. Opt. Soc. Am.* **68**(2): 243–246.

Cerny, D., Bacis, R., Guelachvili, G. & Roux, F. (1978). Extensive analysis of the red system of the CN molecule with a high resolution fourier spectrometer, *J. Mol. Spectrosc.* **73**(1): 154 – 167.

Chalmers, J. & Griffiths, P. (eds) (2002). *Handbook of Vibrational Spectroscopy (5 Volume Set)*, 1 edn, Wiley.

Civiš, S., Kubát, P., Nishida, S. & Kawaguchi, K. (2006). Time-resolved fourier transform infrared emission spectroscopy of $H_3^+$ molecular ion, *Chem. Phys. Lett.* **418**(4-6): 448–453.

Civiš, S., Matulková, I., Cihelka, J., Kawaguchi, K., Chernov, V. E. & Buslov, E. Y. (2010). Time-resolved fourier-transform infrared emission spectroscopy of Au in the 1800–4000-cm$^{-1}$ region: Rydberg transitions, *Phys. Rev. A* **81**(1): 012510.

Civiš, S., Šedivcová-Uhliková, T., Kubelík, P. & Kawaguchi, K. (2008). Time-resolved fourier transform emission spectroscopy of $A^2\Pi$–$X^2\Sigma^+$ infrared transition of the CN radical, *Journal of Molecular Spectroscopy* **250**(1): 20 – 26.

Civiš, S., Matulková, I., Cihelka, J., Kubelík, P., Kawaguchi, K. & Chernov, V. E. (2010). Time-resolved fourier-transform infrared emission spectroscopy of Ag in the (1300–3600)-cm$^{-1}$ region: Transitions involving $f$ and $g$ states and oscillator strengths, *Phys. Rev. A* **82**(2): 022502.

Claeyssens, F., Henley, S. J. & Ashfold, M. N. R. (2003). Comparison of the ablation plumes arising from arf laser ablation of graphite, silicon, copper, and aluminum in vacuum, *J. Appl. Phys.* **94**(4): 2203–2211.

Claeyssens, F., Lade, R. J., Rosser, K. N. & Ashfold, M. N. R. (2001). Investigations of the plume accompanying pulsed ultraviolet laser ablation of graphite in vacuum, *J. Appl. Phys.* **89**(1): 697–709.

Davies, P. B., Guest, M. A. & Stickland, R. J. (1990). Infrared laser spectroscopy of $H_2$ and $D_2$ Rydberg states. I. Application of the polarization model, *J. Chem. Phys.* **93**(8): 5408–5416.

Ding, G. J., Shang, R. C., Chang, L. F., Wen, K. L., Hui, Q. & Chen, D. Y. (1989). Experimental study of Au atom Rydberg states, *J. Phys. B* **22**(10): 1555–1561.

Drossart, P., Maillard, J.-P., Caldwell, J., Kim, S. J., Watson, J. K. G., Majewski, W. A., Tennyson, J., Miller, S., Atreya, S. K., Clarke, J. T., Waite, J. H. & Wagener, R. (1989). Detection of $H_3^+$ on Jupiter, *Nature* **340**(6234): 539–541.

Durry, G. & Guelachvili, G. (1994). $N_2$ (B–A) time-resolved fourier transform emission spectra from a pulsed microwave discharge, *J. Mol. Spectrosc.* **168**(1): 82–91.

Dyubko, S. F., Efremov, V. A., Gerasimov, V. G. & MacAdam, K. (2005). Millimetre-wave spectroscopy of Au I Rydberg states: S, P and D terms, *J. Phys. B* **38**(8): 1107–1118.

Ehrhardt, J. C. & Davis, S. P. (1971). Precision wavelengths and energy levels in gold, *J. Opt. Soc. Am.* **61**(10): 1342–1349.

Furio, N., Ali, A., Dagdigian, P. J. & Werner, H.-J. (1989). Laser excitation of the overlapping CN $B$–$A(8,7)$ and $B$–$X(8,11)$ bands: The relative phase of the $B$–$A$ and $B$–$X$ transition moments, *J. Mol. Spectrosc.* **134**(1): 199 – 213.

George, S., Grays, A. & Engleman, Jr., R. (1988). Spectrum of Au I in the infrared using a fourier-transform spectrometer, *J. Opt. Soc. Am. B* **5**(7): 1500–1502.

Ginter, D. S. & Ginter, M. L. (1988). Multichannel interactions in the $(1\sigma_g)^2(1\sigma_u)ns\sigma, nd\lambda$ ($^3\Sigma_u^+$, $^3\Sigma_u^+$, $^3\Pi_u$, $^3\Pi_u$) Rydberg structures of $He_2$, *J. Chem. Phys.* **88**(6): 3761–3774.

Ginter, D. S., Ginter, M. L. & Brown, C. M. (1984). Multichannel interactions in the $(1\sigma_g)^2(1\sigma_u)np\lambda(^3\Pi_g, ^3\Sigma_g^+)$ Rydberg structures of $He_2$, *J. Chem. Phys.* **81**(12): 6013–6025.

Ginter, M. L. (1965). The spectrum and structure of the $He_2$ molecule: Part III. characterization of the triplet states associated with the UAO's 3*s* and $2p\pi$, *J. Mol. Spectrosc.* **18**(3): 321 – 343.

Gloersen, P. & Dieke, G. H. (1965). Molecular spectra of hydrogen and helium in the infrared, *J. Mol. Spectrosc.* **16**(1): 191–204.

Gomes, A., Aubreton, A., Gonzalez, J. J. & Vacquié, S. (2004). Experimental and theoretical study of the expansion of a metallic vapour plasma produced by laser, *J. Phys. D* **37**(5): 689.

Guelachvili, G. & Rao, K. R. (1986). *Handbook of Infrared Standards: With Spectral Maps and Transition Assignments Between 3 and 2600 µm (v. 1)*, Academic Press.

Hepner, G.; Herman, L. (1956). Nouveau système de bandes d'émission de la molécule $He_2$ vers 4700 $cm^{-1}$, *C. R. Acad. Sci. Paris, Ser. B* **243**(20): 1504–1506.

Herbst, E. & Klemperer, W. (1973). The formation and depletion of molecules in dense interstellar clouds, *Astrophys. J.* **185**: 505–534.

Herzberg, G. & Jungen, C. (1986). The $4f$ states of $He_2$: A new spectrum of $He_2$ in the near infrared, *J. Chem. Phys.* **84**(3): 1181–1192.

Horká, V., Civiš, S., Špirko, V. & Kawaguchi, K. (2004). The infrared spectrum of CN in its ground electronic state, *Collection of Czechoslovak Chemical Communications* **69**(1): 73–89.

Hosaki, Y., Civiš, S. & Kawaguchi, K. (2004). Time-resolved Fourier transform infrared emission spectroscopy of $He_2$ produced by a pulsed discharge, *Chem. Phys. Lett.* **383**(3-4): 256–260.

Huber, K. & Herzberg, G. (1979). *Molecular Spectra and Molecular Structure. IV. Constants of Diatomic Molecules.*, 1 edn, Van Nostrand.

Huntress, Jr., W. T. (1977). Laboratory studies of bimolecular reactions of positive ions in interstellar clouds, in comets, and in planetary atmospheres of reducing composition, *Astrophys. J., Suppl. Ser.* **33**(4): 495–514.

Jannitti, E., Cantù, A. M., Grisendi, T., Pettini, M. & Tozzi, G. P. (1979). Absorption spectrum of Au I in the vacuum ultraviolet, *Phys. Scr.* **20**(2): 156–162.

Kao, L., Oka, T., Miller, S. & Tennyson, J. (1991). A table of astronomically important ro-vibrational transitions for the $H_3^+$ molecular ion, *Astrophys. J., Suppl. Ser.* **77**(2): 317–329.

Kawaguchi, K., Baskakov, O., Hosaki, Y., Hama, Y. & Kugimiya, C. (2003). Time-resolved Fourier transform spectroscopy of pulsed discharge products, *Chem. Phys. Lett.* **369**(3-4): 293–298.

Kawaguchi, K., Hama, Y. & Nishida, S. (2005). Time-resolved Fourier transform infrared spectroscopy: Application to pulsed discharges, *J. Mol. Spectrosc.* **232**(1): 1–13.

Kawaguchi, K., Sanechika, N., Nishimura, Y., Fujimori, R., Oka, T. N., Hirahara, Y., Jaman, A. & Civiš, S. (2008). Time-resolved fourier transform infrared emission spectroscopy of laser ablation products, *Chem. Phys. Lett.* **463**(1–3): 38–41.

Kotlar, A. J., Field, R. W., Steinfeld, J. I. & Coxon, J. A. (1980). Analysis of perturbations in the $A^2\Pi \tilde{} X^2\Sigma^+$ "red" system of CN, *J. Mol. Spectrosc.* **80**(1): 86 – 108.

Lee, W.-B., Wu, J.-Y., Lee, Y.-I. & Sneddon, J. (2004). Recent applications of laser-induced breakdown spectrometry: A review of material approaches, *Appl. Spectrosc. Rev.* **39**(1): 27–97.

Lindsay, C. M. & McCall, B. J. (2001). Comprehensive evaluation and compilation of $H_3^+$ spectroscopy, *J. Mol. Spectrosc.* **210**(1): 60 – 83.

Longmire, M. S., Brown, C. M. & Ginter, M. L. (1980). Absorption spectrum of Cu I between 1570 Å and 2500 Å, *J. Opt. Soc. Am.* **70**(4): 423–429.

Majewski, W. A., Marshall, M. D., McKellar, A. R. W., Johns, J. W. C. & Watson, J. K. G. (1987). Higher rotational lines in the $\nu_2$ fundamental of the $H_3^+$ molecular ion, *J. Mol. Spectrosc.* **122**(2): 341 – 355.

Majewski, W. A., McKellar, A. R. W., Sadovskii, D. & Watson, J. K. G. (1994). New observations and analysis of the infrared vibrationŰrotation spectrum of $H_3^+$, *Can. J. Phys.* **72**(11-12): 1016–1027.

Mantz, A. W. (1976). Infrared multiplexed studies of transient species, *Appl. Spectrosc.* **30**(4): 459–461.

Masutani, K. (2002). *Time-resolved Mid-infrared Spectrometry Using an Asynchronous Fourier Transform Infrared Spectrometer*, Vol. 1 of Chalmers & Griffiths (2002), 1 edn, pp. 655–665.

McCall, B. J., Geballe, T. R., Hinkle, K. H. & Oka, T. (1998). Detection of $H_3^+$ in the Diffuse Interstellar Medium Toward Cygnus OB2 No. 12, *Science* **279**(5358): 1910–1913.

Miotello, A. & Kelly, R. (1999). Laser-induced phase explosion: new physical problems when a condensed phase approaches the thermodynamic critical temperature, *Appl. Phys. A* **69**(Suppl. S): S67–S73. 5th International Conference on Laser Ablation COLA'99, GOTTINGEN, GERMANY, JUL 19-23, 1999.

Motret, O., Pouvesle, J. M. & Stevefelt, J. (1985). Spectroscopic study of the afterglow excited by intense electrical discharges in high-pressure helium hydrogen mixtures, *J. Chem. Phys.* **83**(3): 1095–1100.

Nakanaga, T., Ito, F. & Takeo, H. (1993). Time-resolved high-resolution ftir absorption spectroscopy in a pulsed discharge, *Chem. Phys. Lett.* **206**(1-4): 73 – 76.

Oka, T. (1980). Observation of the infrared spectrum of $H_3^+$, *Phys. Rev. Lett.* **45**(7): 531–534.

Orth, F. B. & Ginter, M. L. (1976). The spectrum and structure of the $He_2$ molecule: Characterization of the triplet states associated with the UAO's $4p\sigma$, $5p\sigma$, and $6p\sigma$, *J. Mol. Spectrosc.* **61**(2): 282 – 288.

Pickering, J. C. & Zilio, V. (2001). New accurate data for the spectrum of neutral silver, *Eur. Phys. J. D* **13**(2): 181–185.

Plašil, R., Glošik, J., Poterya, V., Kudrna, P., Rusz, J., Tichý, M. & Pysanenko, A. (2002). Advanced integrated stationary afterglow method for experimental study of recombination of processes of $H_3^+$ and $D_3^+$ ions with electrons, *Int. J. Mass Spectrom.* **218**(2): 105 – 130.

Platt, J. R. & Sawyer, R. A. (1941). New classifications in the spectra of Au I and Au II, *Phys. Rev.* **60**(12): 866–876.

Prasad, C. V. V. & Bernath, P. F. (1992). Fourier transform jet-emission spectroscopy of the $A^2\Pi_i$–$X^2\Sigma^+$ transition of CN, *J. Mol. Spectrosc.* **156**(2): 327 – 340.

Radziemski, L. J. & Cremers, D. A. (eds) (1989). *Lasers-induced Plasmas and Applications*, Marcel Dekker, New York. Chap. 7, pp. 295–325.

Ralchenko, Y., Kramida, A., Reader, J. & Team, N. (2008). NIST atomic spectra database (version 3.1.5).

Ram, R., Davis, S., Wallace, L., Engleman, R., Appadoo, D. & Bernath, P. (2006). Fourier transform emission spectroscopy of the $B^2\Sigma^+$–$X^2\Sigma^+$ system of CN, *J. Mol. Spectrosc.* **237**(2): 225 – 231.

Rehfuss, B. D., Suh, M.-H., Miller, T. A. & Bondybey, V. E. (1992). Fourier transform UV, visible, and infrared spectra of supersonically cooled CN radical, *J. Mol. Spectrosc.* **151**(2): 437 – 458.

Rödig, C. & Siebert, F. (2002). *Fast Time-resolved Mid-infrared Spectroscopy Using an Interferometer*, Vol. 1 of Chalmers & Griffiths (2002), 1 edn, pp. 625–Ű640.

Rogers, S. A., Brazier, C. R., Bernath, P. F. & Brault, J. W. (1988). Fourier transform emission spectroscopy of the $b^3\Pi_g$–$a^3\Sigma_u^+$ transition of $He_2$, *Mol. Phys.* **63**(5): 901–908.

Rossa, M., Rinaldi, C. A. & Ferrero, J. C. (2009). Internal state populations and velocity distributions of monatomic species ejected after the 1064 nm laser irradiation of barium, *J. Appl. Phys.* **105**(6): 063306.

Rubahn, H.-G. (1999). *Laser Applications in Surface Science and Technology*, Wiley, New York.

Safronova, U. I., Savukov, I. M., Safronova, M. S. & Johnson, W. R. (2003). Third-order relativistic many-body calculations of energies and lifetimes of levels along the silver isoelectronic sequence, *Phys. Rev. A* **68**(6): 062505.

Sharp, C. M. (1984). The computation of Franck–Condon factors, *r*-centroids and associated quantities in the electronic transitions of diatomic molecules, *Astron. Astrophys. Suppl. Ser.* **55**: 33–50.

Shenstone, A. G. (1940). The arc spectrum of silver, *Phys. Rev.* **57**(10): 894–898.

Shenstone, A. G. (1948). The first spectrum of copper (Cu I), *Philos. Trans. R. Soc. London, Ser. A* **241**(832): 297–322.

Smith, G. D. & Palmer, R. A. (2002). *Instrumental Aspects of Time-resolved Spectra Generated Using Step-scan Interferometers*, Vol. 1 of Chalmers & Griffiths (2002), 1 edn, pp. 641–Ű654.

Solka, H., Zimmermann, W., Stahn, A., Reinert, D. & Urban, W. (1987). Observation of the $B^3\Pi_u$–$A^3\Sigma_g^+$ band of $He_2$, *Mol. Phys.* **60**(5): 1179–1182.

Strasser, D., Lammich, L., Kreckel, H., Krohn, S., Lange, M., Naaman, A., Schwalm, D., Wolf, A. & Zajfman, D. (2002). Breakup dynamics and the isotope effect in $H_3^+$ and $D_3^+$ dissociative recombination, *Phys. Rev. A* **66**(3): 032719.

Vertes, A., Dreyfus, R. W. & Platt, D. E. (1994). Modeling the thermal-to-plasma transitions for Cu photoablation, *IBM J. Res. Dev.* **38**(1): 3–10.

Vervloet, M. & Watson, J. K. (2003). Improved infrared and visible emission spectra of the $H_3$ and $D_3$ molecules, *Journal of Molecular Spectroscopy* **217**(2): 255 – 277.

Zhankui, J., Jönsson, P., Larsson, J. & Svanberg, S. (1990). Studies on radiative lifetimes in the $4d^{10}ns\ ^2S$ and $4d^{10}nd\ ^2D$ sequences of neutral silver, *Z. Phys. D* **17**(1): 1–14.

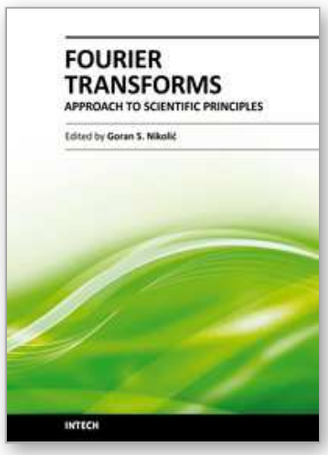


**Fourier Transforms - Approach to Scientific Principles**
Edited by Prof. Goran Nikolic

ISBN 978-953-307-231-9
Hard cover, 468 pages
**Publisher** InTech
**Published online** 11, April, 2011
**Published in print edition** April, 2011

This book aims to provide information about Fourier transform to those needing to use infrared spectroscopy, by explaining the fundamental aspects of the Fourier transform, and techniques for analyzing infrared data obtained for a wide number of materials. It summarizes the theory, instrumentation, methodology, techniques and application of FTIR spectroscopy, and improves the performance and quality of FTIR spectrophotometers.



**InTech Europe**
University Campus STeP Ri
Slavka Krautzeka 83/A
51000 Rijeka, Croatia
Phone: +385 (51) 770 447
Fax: +385 (51) 686 166
www.intechopen.com

**InTech China**
Unit 405, Office Block, Hotel Equatorial Shanghai
No.65, Yan An Road (West), Shanghai, 200040, China
中国上海市延安西路65号上海国际贵都大饭店办公楼405单元
Phone: +86-21-62489820
Fax: +86-21-62489821

IntechOpen